scientific reports

Check for updates

OPEN

Probing into 9′-substituted Suzuki-coupled noscapine ionic liquids as potent microtubule targeting anticancer agents with hemoglobin affinity

Shubham Sewariya[1,2,6], Nistha Mishra[1,3], Sagar Panchal[1], Shrikant Kukreti[1] & Ramesh Chandra[1,4,5,6]✉

On a global scale, lung cancer accounts for 18% of all cancer deaths making it the most lethal cancer. To restrain this, there has been continual research in the domain of microtubule-targeting anticancer agents but issues like toxicity, immunosuppression, effective delivery to tumor site, etc. persist to impede their clinical success. Unlike the other existing drugs in this regime; noscapine (a non-opioid alkaloid) is testified to be an intrinsically safer drug with minimal side effects. In this work, we have synthesized and evaluated novel 9′-substituted suzuki-coupled noscapine ionic liquid(s) as effectual anticancer drug(s) against non-small cell (H1299) lung cancer. We have devised a synthetic route (employed suzuki coupling for subsuming the biaryl pharmacophore and combined it with the idea of active pharmaceutical ingredient-based ionic liquids (API-ILs)) to yield the desired API-ILs followed by their characterization using associated analytical techniques like NMR, HRMS, etc. Following this, we have performed SAR analysis of the API-ILs using molecular docking with the target tubulin protein and preliminary in vitro screening against H1299 (non-small cancer) cells to opt for the most promising analogue i.e., [*p*-NO_2-Nos]I. Upon finding the most potent ionic liquid, we carried out MD simulations and MM-PBSA/GBSA calculations to get an insight into its interaction with tubulin and human hemoglobin using computational and spectroscopic studies respectively. From computational studies, we inferred that [*p*-NO_2-Nos]I forms a stable complex with tubulin mainly driven by non-polar interactions. From spectroscopic studies, we disclosed that [*p*-NO_2-Nos]I binds to human hemoglobin (Hb) in a 1:1 stoichiometric ratio with a binding constant (K_b) of ~ 1.38×10^5 M^{-1} at 298 K. Finally, we have examined the cytotoxicity of [*p*-NO_2-Nos]I against H1299 cancer cell line and compared it to [9-Br-Nos]IBr_2, noscapine and Paclitaxel. The IC_{50} values for [*p*-NO_2-Nos]I came out to be 67.84 ± 4.84 µM at 48 h and 19.67 ± 3.1µM at 72 h, both of which were significantly lower than [9-Br-Nos]IBr_2 and Noscapine. The potent [*p*-NO_2-Nos]I was further screened using A549 cell line and similar results were observed relative to H1299 cell line. Overall, these findings envelop the potential of such enhanced spindle poisons against lung cancer.

Keywords Noscapine, Microtubules, Hemoglobin, API-IL, Lung cancer, Biaryl pharmacophore

In the 21st century, cancer continues to be one of the most formidable challenges to human health. Based on the recent GLOBOCAN estimates by International Agency for Research on Cancer (IARC), it was solely responsible for 9.7 million deaths in the year 2022[1]. The same report also displays that lung cancer was the most incident as well as the most fatal cancer in that year leading up to 2.5 million new cases and 1.8 million deaths globally. The alarming statistics demand constant search and development of novel anticancer therapeutics against lung cancer. In this domain, spindle poisons or microtubule-targeting drugs[2], oncolytic peptides[3–5], ionic liquids, etc.

[1]Department of Chemistry, University of Delhi, Delhi 110007, India. [2]School of Pharmacy and Biomedical Sciences, University of Central Lancashire, Preston PR1 7QT, UK. [3]Department of Biotechnology, Delhi Technological University, Delhi 110042, India. [4]Dr. B. R. Ambedkar Center for Biomedical Research, University of Delhi, Delhi 110007, India. [5]Institute of Nano Medical Sciences, University of Delhi, Delhi 110007, India. [6]Maharaja Surajmal Brij University, Rajasthan 321201, India. ✉email: acbrdu@hotmail.com; rameshchandragroup@gmail.com

have emerged as effective cytotoxic agents against non-small cell lung cancer. Microtubules are a crucial target for chemotherapeutic agents because any dysregulation in microtubule dynamics (stabilization or destabilization) induces hinderance in spindle formation during mitosis which further leads to cell apoptosis[6].

Nature is a rich source of such microtubule targeting anticancer drugs[7] namely vinca alkaloids, eribulin, maitansine, estramustine, taxanes etc. (Fig. 1) The obstacles in the clinical success of these existing drugs are high lipophilicity, associated adverse side effects and effective delivery to the tumor site. Apart from this, drug resistance is another vital reason to focus on much-needed development of novel anticancer agents. To this end, noscapine is a benzylisoquinoline alkaloid that has been well-documented to stabilize the microtubule dynamics resulting in inhibition of cancer cells proliferation[8–11]. Noscapine is an intrinsically safer and task-specific anticancer agent as it upholds primary immune response and exhibits minimum toxicity[11]. Over the years, researchers have emphasized on the importance of biaryl pharmacophore in drugs for their antineoplastic activity[12–14]. In line with this, various Suzuki-coupled noscapine analogues have been assessed for better pharmacokinetic properties in recent years[15–17].

Based on these reports combined with the observation that roughly 50% of the marketed drugs are administrated as salts, we proposed to develop and evaluate novel 9'-substituted suzuki-coupled noscapine based ionic liquids. Ionic liquids are salts, generally composed of organic cations and organic or inorganic counter anions. We aimed at the notion of ionic liquids because of their potential in improving vital properties like solubility, bioavailability, drug delivery etc. of a drug candidate[18,19]. The intended noscapine-based ionic liquids fall under the category of active pharmaceutical ingredient based ionic liquids (API-ILs) i.e., third generation of ionic liquids[20]. Various possible combinations in API-ILs allow fine-tuning of their associated properties and the same have been screened for their anticancer profiles[21,22]. In our previous work, we outlined the enhanced potency of 9-bromo noscapine ionic liquid over noscapine as an anticancer agent against non-small cell lung cancer[23].

Herein, we report the synthesis of novel 9'-substituted suzuki-coupled noscapine ionic liquids (Scheme 1) and the assessment of most promising analogue i.e., [*p*-NO_2-Nos]I as an efficacious anticancer drug against non-small cell lung cancer. Firstly, as proof of concept, we carried out preliminary molecular docking and in vitro screening for all synthesized analogues and opted for the most desired API-IL i.e., [*p*-NO_2-Nos]I. We then performed the computational studies for investigating the interaction of [*p*-NO_2-Nos]I with the target tubulin protein in depth. Next, we probed into the biophysical interaction of [*p*-NO_2-Nos]I with human hemoglobin (Hb) using spectroscopic techniques as Hb is the most abundant plasma protein and a natural drug carrier. Moreover, there have been significant advancements in development of Hb-encapsulated nanoparticles for drug transport to tumor site[24–26]. In this area, we have reported the binding of other noscapine ionic liquids with proteins like BSA, ct-DNA, Hb in the past[27–30]. Lastly, we screened the synthesized [*p*-NO_2-Nos]I against H1299 cell line (non-small cell lung cancer) for its bioactivity and compared it to the parent compound.

Chemistry

Materials and methods

All the purchased reagents and solvents were analytically pure and used without any further purification. The lyophilized powder of human hemoglobin, (S, R)-Noscapine and $Pd(PPh_3)_4$ were purchased from Sigma Aldrich whereas Alfa Aesar, TCI, and SRL were the sources for all other chemicals and solvents utilized in this work.

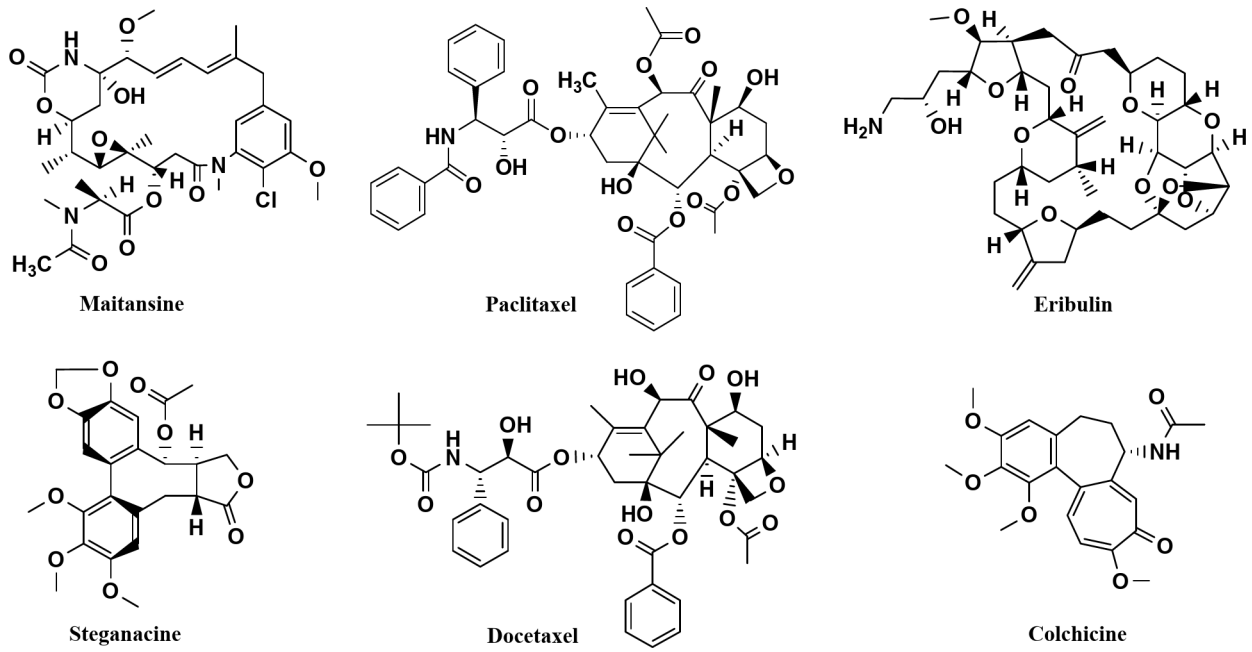

Fig. 1. Some microtubule-targeting anticancer drugs from nature.

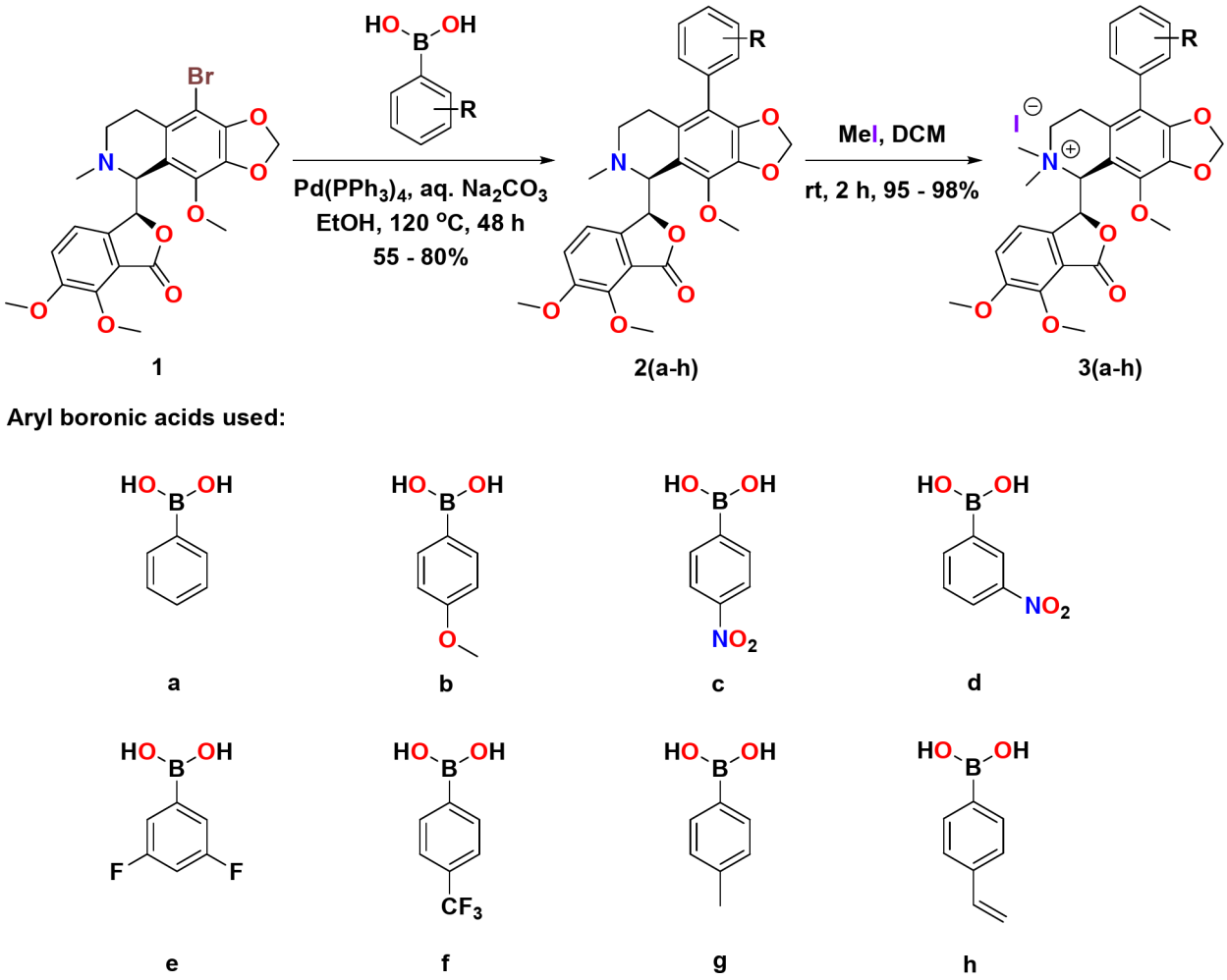

Scheme 1. Synthetic route to obtain 9'-substituted suzuki-coupled noscapine ionic liquids.

The progression of the reactions was monitored through thin layer chromatography on pre-coated Merck 5554 Kieselgel 60 F_{254} plates using Hexane: Ethyl Acetate = 7:3 mobile phase and the spots were visualized under UV-light of 366 nm. Column chromatography was performed on silica gel 60 (Mesh 230–400 ASTM, grading 0.04–0.063) as stationary phase. All characterization studies were carried out at University Science Instrumentation Centre (USIC), University of Delhi. The ^{1}H and ^{13}C NMR spectra were recorded in $CDCl_3$ on a Bruker Avance Neo NMR at 400 MHz and 100 MHz respectively. The high-resolution mass spectral data was obtained using an Agilent Technology-6530, Accurate mass, Q-TOF LCMS spectrometer.

Synthesis of 9′-substituted Suzuki-coupled noscapine ionic liquids

Procedure for the synthesis of 9'-substituted Suzuki-coupled noscapinoids

In an oven-dried round bottom flask, 9-bromo noscapine **1** (1 eq.) was dissolved in ethanol: H_2O (1:1). To this solution, $Pd(PPh_3)_4$ (10 mol%); respective aryl boronic acid(s) (1.2 eq, Scheme 1); Na_2CO_3 (2 eq.) were added sequentially. The reaction mixture (RM) was then refluxed at a temperature of 120 ℃ for 48 h. Upon completion of reaction, the RM was brought to room temperature and the organic solvents were evaporated under reduced pressure. Subsequently, the organic layer was extracted by adding chloroform 2–3 times (aqueous NaOH work-up). The filtrate was dried over anhydrous Na_2SO_4 and concentrated under vacuum to give crude. The crude was then purified using column chromatography over silica gel (25–30% ethyl acetate in hexane) to give **2(a-h)** as pure compounds. The NMR and mass spectra of the compounds are included in the supporting information (Figure S1–S16).

Procedure for the synthesis of 9'-substituted Suzuki-coupled noscapine ILs

In an oven-dried round bottom flask, the respective compound **2(a-h)** was dissolved in dichloromethane and upon dissolution, methyl iodide (6.5 eq.) was added dropwise to the solution. The reaction mixture was then allowed to stir at room temperature for 2 h. Upon completion of reaction, the solvent was removed under reduced pressure and the crude was washed with ethyl acetate 3–4 times wherein it was decanted. Later, the crude was dissolved in chloroform and concentrated in vacuum to give pure compounds **3(a-h)** as shown in Scheme 1. The NMR and mass spectra of the compounds are included in the supporting information (Figure

S17–S32). The EDAX spectrum of **3c** is given in the supporting information (Figure S33) to confirm the presence of iodine in API-ILs.

(S)−5-((S)−4,5-dimethoxy-3-oxo-1,3-dihydroisobenzofuran-1-yl)−4-methoxy-6,6-dimethyl-9-phenyl-5,6,7,8-tetrahydro-[1,3]dioxolo[4,5-g]isoquinolin-6-ium iodide ***(3a)*** Appearance: Dark brown amorphous product; Yield: 95%; m.p.: 81–83 °C; ^{1}H NMR (400 MHz, CDCl3) δ 8.08 (d, J = 7.3 Hz, 1H), 7.62–7.46 (m, 2 H), 7.39–7.36 (m, 2 H), 7.32–7.26 (m, 2 H), 6.22 (s, 2 H), 5.77 (d, J = 1.4 Hz, 1H), 5.67 (d, J = 1.3 Hz, 1H), 4.12 (s, 3 H), 3.94–3.91 (m, 1H), 3.87 (s, 3 H), 3.85 (s, 3 H), 3.85–3.81 (m, 1H), 3.49 (s, 3 H), 3.37 (s, 3 H), 3.19–3.12 (m, 1H), 2.66–2.57 (m, 1H); ^{13}C NMR (100 MHz, CDCl3) δ 165.36, 151.95, 147.30, 146.31, 138.30, 135.96, 132.29, 131.85, 131.11, 128.74, 127.88, 127.28, 123.60, 120.58, 117.99, 116.22, 106.78, 100.29, 74.17, 67.24, 61.18, 58.17, 56.90, 55.83, 52.79, 22.31; HR-MS calculated for $[C_{29}H_{30}NO_7]^+$ $[M]^+$: 504.20, found: 504.20.

(S)−5-((S)−4,5-dimethoxy-3-oxo-1,3-dihydroisobenzofuran-1-yl)−4-methoxy-9-(4-methoxyphenyl)−6,6-dimethyl-5,6,7,8-tetrahydro-[1,3]dioxolo[4,5-g]isoquinolin-6-ium iodide ***(3b)*** Appearance: Pale brown amorphous product; Yield: 96%; m.p.: 97–99 °C; ^{1}H NMR (400 MHz, $CDCl_3$) δ 7.60–7.55 (m, 2 H), 7.46 (d, *J* = 6.2 Hz, 1H), 7.39 (d, *J* = 6.2 Hz, 1H), 6.78 (d, *J* = 5.6 Hz, 2 H), 6.27 (s, 2 H), 5.76 (d, *J* = 1.4 Hz, 1H), 5.68 (d, *J* = 1.4 Hz, 1H), 4.13 (s, 3 H), 3.96–3.93 (m, 1H), 3.84 (s, 3 H), 3.83 (s, 3 H), 3.82 (s, 3 H), 3.79–3.76 (m, 1H), 3.44 (s, 3 H), 3.37 (s, 3 H), 3.14–3.08 (m, 1H), 2.71–2.64 (m, 1H); ^{13}C NMR (100 MHz, $CDCl_3$) δ 166.44, 161.87, 152.92, 148.16, 147.23, 139.78, 135.15, 133.22, 132.07, 128.60, 125.00, 121.46, 119.10, 117.26, 114.65, 113.24, 108.28, 101.47, 75.19, 68.22, 62.27, 62.09, 59.12, 56.90, 53.80, 52.25, 22.66; HR-MS calculated for $[C_{30}H_{32}NO_8]^+$ $[M]^+$: 534.21, found: 534.21.

(S)−5-((S)−4,5-dimethoxy-3-oxo-1,3-dihydroisobenzofuran-1-yl)−4-methoxy-6,6-dimethyl-9-(4-nitrophenyl)−5,6,7,8-tetrahydro-[1,3]dioxolo[4,5-g]isoquinolin-6-ium iodide ***(3c)*** Appearance: Pale brown amorphous product; Yield: 97%; m.p.: 95–97 °C; ^{1}H NMR (400 MHz, $CDCl_3$) δ 8.22 (d, *J* = 8.2 Hz, 2 H), 7.59 (d, *J* = 8.2 Hz, 2 H), 7.46 (d, *J* = 8.0 Hz, 1H), 7.28 (d, *J* = 8.0 Hz, 1H), 6.26 (s, 2 H), 5.80 (d, J = 1.4 Hz, 1H), 5.69 (d, J = 1.3 Hz, 1H), 4.13 (s, 3 H), 3.99–3.94 (m, 1H), 3.87 (s, 3 H), 3.85 (s, 3 H), 3.81–3.77 (m, 1H), 3.49 (s, 3 H), 3.38 (s, 3 H), 3.19–3.12 (m, 1H), 2.73–2.64 (m, 1H); ^{13}C NMR (100 MHz, $CDCl_3$) δ 166.47, 153.06, 148.36, 147.58, 140.05, 136.85, 132.14, 132.04, 131.24, 128.61, 128.49, 124.38, 124.01, 121.52, 119.11, 117.22, 108.41, 101.61, 75.16, 68.13, 62.15, 59.20, 57.61, 56.88, 53.85, 22.70; HR-MS calculated for $[C_{29}H_{29}N_2O_9]^+$ $[M]^+$: 549.18, found: 549.18.

(S)−5-((S)−4,5-dimethoxy-3-oxo-1,3-dihydroisobenzofuran-1-yl)−4-methoxy-6,6-dimethyl-9-(3-nitrophenyl)−5,6,7,8-tetrahydro-[1,3]dioxolo[4,5-g]isoquinolin-6-ium iodide ***(3d)*** Appearance: Orange amorphous product; Yield: 97%; m.p.: 95–97 °C; ^{1}H NMR (400 MHz, $CDCl_3$) δ 8.18 (d, *J* = 7.7 Hz, 1H), 8.10 (s, 1H), 7.53–7.46 (m, 4 H), 6.24 (s, 2 H), 5.79 (d, *J* = 1.4 Hz, 1H), 5.70 (d, *J* = 1.4 Hz, 1H), 4.10 (s, 3 H), 4.00–3.96 (m, 1H), 3.88 (s, 3 H), 3.85 (s, 3 H), 3.82–3.77 (m, 1H), 3.50 (s, 3 H), 3.35 (s, 3 H), 3.17–3.13 (m, 1H), 2.74–2.61 (m, 1H); ^{13}C NMR (100 MHz, $CDCl_3$) δ 165.49, 151.95, 147.41, 146.26, 138.96, 135.57, 134.17, 132.32, 131.87, 130.84, 128.96, 128.33, 125.18, 124.00, 120.32, 118.13, 116.24, 107.46, 101.24, 74.20, 67.19, 61.11, 58.16, 56.30, 55.88, 52.79, 22.41; HR-MS calculated for $[C_{29}H_{29}N_2O_9]^+$ $[M]^+$: 549.19, found: 549.19.

(S)−9-(3,5-difluorophenyl)−5-((S)−4,5-dimethoxy-3-oxo-1,3-dihydroisobenzofuran-1-yl)−4-methoxy-6,6-dimethyl-5,6,7,8-tetrahydro-[1,3]dioxolo[4,5-g]isoquinolin-6-ium iodide ***(3e)*** Appearance: Pale brown amorphous product; Yield: 96%; m.p.: 90–92 °C; ^{1}H NMR (400 MHz, $CDCl_3$) 7.47–7.25 (m, 2 H), 7.05–6.92 (m, 1H), 6.77 (d, *J* = 7.4 Hz, 2 H), 6.25 (s, 2 H), 5.77 (d, *J* = 1.4 Hz, 1H), 5.70 (d, *J* = 1.4 Hz, 1H), 4.11 (s, 3 H), 3.99–3.95 (m, 1H), 3.87 (s, 3 H), 3.85 (s, 3 H), 3.81–3.77 (m, 1H), 3.48 (s, 3 H), 3.35 (s, 3 H), 3.20–3.13 (m, 1H), 2.73–2.62 (m, 1H) ; ^{13}C NMR (100 MHz, $CDCl_3$) δ 166.48, 164.26, 153.07, 148.29, 147.52, 137.09, 135.17, 132.88, 131.79, 125.04, 123.95, 121.56, 119.32, 117.24, 113.22, 107.83, 102.24, 101.49, 75.15, 66.73, 62.09, 59.18, 57.66, 56.92, 53.92, 22.62; HR-MS calculated for $[C_{29}H_{28}F_2NO_7]^+$ $[M]^+$: 540.18, found: 540.18.

(S)−5-((S)−4,5-dimethoxy-3-oxo-1,3-dihydroisobenzofuran-1-yl)−4-methoxy-6,6-dimethyl-9-(4-(trifluoromethyl)phenyl)−5,6,7,8-tetrahydro-[1,3]dioxolo[4,5-g]isoquinolin-6-ium iodide ***(3f)*** Appearance: Pale brown amorphous product; Yield: 98%; m.p.: 95–97 °C; ^{1}H NMR (400 MHz, $CDCl_3$) δ 7.63 (d, *J* = 7.6 Hz, 2 H), 7.54 (d, *J* = 7.8 Hz, 1H), 7.36 (d, *J* = 7.5 Hz, 2 H), 7.27 (d, *J* = 7.1 Hz, 1H), 6.23 (s, 2 H), 5.77 (d, *J* = 1.4 Hz, 1H), 5.69 (d, *J* = 1.4 Hz, 1H), 4.10 (s, 3 H), 3.99–3.94 (m, 1H), 3.87 (s, 3 H), 3.84 (s, 3 H), 3.81–3.72 (m, 1H), 3.47 (s, 3 H), 3.36 (s, 3 H), 3.16–3.10 (m, 1H), 2.67–2.60 (m, 1H); ^{13}C NMR (100 MHz, $CDCl_3$) δ 165.43, 151.97, 147.31, 146.30, 138.72, 135.75, 134.19, 132.30, 129.72, 129.42, 124.77, 124.00, 123.50, 121.60, 120.54, 118.06, 116.21, 107.15, 100.45, 74.16, 67.15, 61.14, 58.14, 56.63, 55.83, 52.80, 22.41; HR-MS calculated for $[C_{30}H_{29}F_3NO_7]^+$ $[M]^+$: 572.18, found: 572.18.

(S)−5-((S)−4,5-dimethoxy-3-oxo-1,3-dihydroisobenzofuran-1-yl)−4-methoxy-6,6-dimethyl-9-(p-tolyl)−5,6,7,8-tetrahydro-[1,3]dioxolo[4,5-g]isoquinolin-6-ium iodide ***(3 g)*** Appearance: Yellow amorphous product; Yield: 95%; m.p.: 82–84 °C; ^{1}H NMR (400 MHz, $CDCl_3$) δ 8.01 (d, *J* = 7.8 Hz, 2 H), 7.27 (d, *J* = 8.2 Hz, 2 H), 7.17 (d, *J* = 7.9 Hz, 1H), 7.08 (d, *J* = 7.9 Hz, 1H), 6.28 (s, 2 H), 5.78 (d, *J* = 1.3 Hz, 1H), 5.67 (d, *J* = 1.3 Hz, 1H), 4.12 (s, 3 H), 3.90–3.85 (m, 1H), 3.83 (s, 6 H), 3.79–3.65 (m, 1H), 3.39 (s, 3 H), 3.36 (s, 3 H), 3.11–3.07 (m, 1H), 2.77–2.62 (m, 1H), 2.31 (s, 3 H); ^{13}C NMR (100 MHz, $CDCl_3$) δ 166.35, 152.88, 150.64, 147.32, 140.00, 137.37, 135.18, 133.60, 129.85, 129.59, 126.28, 125.01, 121.31, 119.19, 117.13, 107.73, 102.28, 101.23, 75.27, 68.69, 62.15, 59.01, 56.92, 53.99, 52.07, 23.41, 22.67; HR-MS calculated for $[C_{30}H_{32}NO_7]^+$ $[M]^+$: 518.21, found: 518.21.

(S)−5-((S)−4,5-dimethoxy-3-oxo-1,3-dihydroisobenzofuran-1-yl)−4-methoxy-6,6-dimethyl-9-(4-vinylphenyl)−5,6,7,8-tetrahydro-[1,3]dioxolo[4,5-g]isoquinolin-6-ium iodide ***(3 h)*** Appearance: Yellow amorphous product; Yield: 96%; m.p.: 84–86 °C; ^{1}H NMR (400 MHz, $CDCl_3$) δ 7.70–7.57 (m, 4 H), 7.47 (d, *J* = 7.0 Hz, 1H), 7.27 (d, *J* = 7.6 Hz, 1H), 6.67 (dd, *J* = 17.3, 10.8 Hz, 1H), 6.25 (s, 2 H), 5.77–5.66 (m, 3 H), 5.23 (d, *J* = 10.8 Hz, 1H), 4.05 (s, 3 H), 3.95–3.90 (m, 1H), 3.87 (s, 3 H), 3.84 (s, 3 H), 3.80–3.78 (m, 1H), 3.49 (s, 3 H), 3.32 (s, 3 H), 3.22–3.18 (m, 1H), 2.70–2.61 (m, 1H); ^{13}C NMR (100 MHz, $CDCl_3$) δ 166.86, 151.96, 147.37, 146.31, 138.35, 136.58, 135.20, 134.18, 131.03, 128.98, 127.47, 125.65, 123.99, 120. 50, 120.11, 118.03, 116.21, 113.05, 107.17,

101.27, 74.13, 67.12, 61.16, 58.19, 57.06, 55.81, 52.84, 22.41; HR-MS calculated for $[C_{31}H_{32}NO_7]^+$ $[M]^+$: 530.21, found: 530.21.

In-silico modelling studies

Molecular Docking and molecular dynamics (MD) simulations

Molecular docking was done using AutoDock Vina v1.2.3[31]. The 3D structure of ligand was made using Chem3D Pro 16.0 and energy minimization were done using an inbuilt MM2 force field with RMS gradient of 0.010[32]. The 3D crystal structure of Tubulin was obtained from the Protein Data Bank (https://www.rcsb.org/) (PDB ID – 1TUB)[33,34]. Different tools were used for the preparation and analysis of the ligand-protein interaction namely, Biovia Discovery Studio 2021 client[35], Pymol[36]and Autodock Tools-1.5.6[37]. Missing residues of the protein were corrected by AutoDock Tools-1.5.6. During preparation of the protein for docking, all the H_2O and other ligands presented in the raw .pdb file were removed and then non-polar hydrogens were added to the crystal structure of protein. Now, charge on protein was neutralized by using Kollman followed by the Gasteiger charge and the resultant file was saved in .pdb format. The size and position details of the grid on the protein are given in the supporting information (**Table S1**). After docking, the ligand and protein were merged and further utilized for Molecular Dynamics (MD) simulation studies. MD simulation was done using GROMACS-2023.1 package using Amber99SB-ILDN protein, nucleic AMBER94 force field[38–46]. Antechamber and Acpype were used to obtain the topology of the ligand and maintain the charge on the ligand[47–50]. System was then solvated with TIP3P and neutralized using NaCl by replacing 17 solvent molecules with Na atoms. Energy minimization of the system was done by the MD (Leap-Frog integrator) method followed by 1000 ps NVT simulation and equilibration at 300 K and 1 atm pressure for 1000 ps NPT simulation. To maintain the temperature and pressure of the system during the simulation, we used the V-rescale thermostat and Berendsen's pressure coupling algorithm, respectively. MD simulation of 10,000 ps (10 ns) was executed and different analysis were done using in-built Gromacs modules.

Binding free energy calculations MMPBSA/GBSA

After successfully getting the trajectories from MD simulations, these trajectories were further used to calculate the binding free energy using Molecular mechanics Poisson-Boltzmann surface area/Generalized-Born surface area (MMPBSA/GBSA)[51–54]. This is a very versatile and one the most used method that allows to assess the binding free energy, stability of the structure throughout the MD calculation and evaluate the contribution of each individual residue present on the receptor by free energy decomposition studies.

In this method the change in binding free energy can be calculated by using Eq. 1.

$$\Delta G_{bind} = < G_{COM} > - < G_{REC} > - < G_{LIG} > \quad (1)$$

Each term on the right-hand side can be calculated using the following Eq. 2.

$$< G_x > = < E_{MM} > + < G_{sol} > - < TS > \quad (2)$$

which can also be written as

$$\Delta G_{bind} = \Delta H - T\Delta S \quad (3)$$

where ΔG is change in Gibb's free energy, ΔH represents enthalpy of binding and ΔS corresponds to the conformational entropy after ligand binds with the receptor.

Spectroscopic studies

A 1X phosphate buffer (PBS) with a pH of 7.4 was used for all biophysical experiments. A 2.5 µM Hb stock solution was prepared and kept at 4 °C until use. This solution was utilized for UV-Visible and fluorescence spectroscopy, whereas a more diluted sample with a concentration of 1 µM was used for circular dichroism spectroscopy.

UV-Visible spectroscopy

To probe into [*p*-NO_2-Nos]I-Hb interaction, we recorded the UV-Visible spectra on a Thermo Scientific Evolution 300 UV-Vis spectrophotometer. For the experiment, quartz cuvettes (1 cm path length) were used, and the spectra were recorded in the wavelength range of 200–500 nm at 298 K. 1X PBS solution was used as the reference solution during the experiment. We recorded the absorbance at a constant 5×10^{-6} M concentration of Hb and then upon adding [*p*-NO_2-Nos]I from 0 to 50 µM at a pH of 7.4.

Fluorescence spectroscopy

We recorded the fluorescence spectra on Hitachi F-7000 Fluorescence Spectrophotometer. Firstly, we recorded the spectrum of hemoglobin and subsequently titrated with increasing concentrations of [*p*-NO_2-Nos]I from 0 to 45 µM. The experiment was carried out at three different temperatures i.e., 298 K, 303 K and 308 K while maintaining a pH of 7.4. For these experiments, the excitation wavelength was fixed at 280 nm and the emission spectra ranged from 300 nm to 500 nm; the slit widths were set at 5 nm and the samples were scanned at a rate of 2400 nm/min.

For appropriate evaluation of the spectral data, we accounted for the inner filter effect (reduction of fluorescence intensity due to ligand's absorbance at the excitation or emission wavelength) and corrected it by applying the following Eq. (4):

$$F_{corrected} = F_{observed}.e^{(Aex+Aem)/2} \quad (4)$$

Herein, $F_{observed}$ and $F_{corrected}$ denote the observed fluorescence and corrected fluorescence of hemoglobin respectively. A_{ex} is the absorption of the ionic liquid at excitation wavelength and A_{em} is the absorption of ionic liquid at emission wavelengths of hemoglobin.

Circular dichroism spectroscopy

We recorded the far-UV CD spectra on a Jasco J-815 spectrophotometer. Initially, we recorded the hemoglobin spectrum and then titrated with stepwise increasing concentrations of [*p*-NO_2-Nos]I from 0 to 5 µM. During the experiment, we used quartz cuvettes of path length of 1 cm; maintained a pH of 7.4 and temperature at 298 K. All the spectra were obtained in the wavelength range of 190 nm to 250 nm. The samples were scanned at a speed of 100 nm/min while fluxing nitrogen throughout the experiment.

Biology

Cell culture and reagents

All the chemicals were purchased from Sigma Aldrich, SRL and [*p*-NO_2-Nos]I ionic liquid was obtained from Scheme 1. The H1299 and A549 (non-small human lung cancer) cell line was obtained from National Centre for Cell Science (NCCS), Pune, India. Dulbecco's modified eagle medium (1X DMEM) was utilized for preparing the media and was supplemented with 4.5 g/L glucose, 1% antibiotic and 10% fetal bovine serum (FBS) for cell cultivation. The cells were incubated at a 5% CO_2 concentration in humidified atmosphere and a temperature of 37 ℃ for culture. The stock solutions of noscapine, [9-Br-Nos]IBr_2, [*p*-NO_2-Nos]I and Paclitaxel were prepared to be 20×10^3 µM in DMSO.

In vitro cell proliferation assay

The colorimetric 3-(4,5-dimethylthiazol-2-yl)−2,5-diphenyltetrazolium bromide (MTT) assay was used for assessing the inhibition of cell proliferation in H1299 and A549 cell line. The cancer cells were harvested using trypsin & then seeded into 96-well microplates with ~10×10^3 cells/well. Upon seeding, they were incubated in culture medium at a 5% CO_2 concentration in humidified atmosphere at 37 ℃ temperature for 24 h. The cultured cells were treated with gradient concentrations of noscapine (0–100 µM), [9-Br-Nos]IBr_2 (0–100 µM) and [*p*-NO_2-Nos]I (0–100 µM) separately and incubated for 48 h and 72 h under the same conditions. For a separate experiment, [*p*-NO_2-Nos]I & Paclitaxel (0–10 µM) was taken and incubated under the same conditions. After the stated incubation time, the media was removed and each well was washed with PBS buffer. Next, 100 µl of MTT solution (0.5 $mgml^{-1}$ dissolved in DMEM) was poured in each well and the cells were incubated for 3 hours at 5% CO_2, 37 ℃. Post-incubation, MTT solution was aspirated from the wells and the crystals obtained were dissolved in 100µL of DMSO. The absorbance of each well was recorded using BioTek Epoch 2 microplate spectrophotometer at an optical density of 570 nm. A plot of the percentage of viable cells as a function of drug concentration was used to compare the treated and control groups and determine the IC_{50} value (drug concentration required to prevent 50% cell proliferation) for noscapine, [9-Br-Nos]IBr_2 and [*p*-NO_2-Nos]I. The experiments were conducted in triplicate.

Results and discussion

General

Suzuki coupling is the palladium catalyzed cross-coupling reaction between aryl halides and aryl boronic acids using an aqueous base. It is one of the top reactions exploited for the synthesis of drug leads in medicinal chemistry via introduction of the biaryl pharmacophore (Csp^2 – Csp^2 bond formation). The manifold benefits of this reaction include mild reaction conditions, use of environmentally safer boronic acids relative to other organometallic reagents, air and moisture stability, etc[55]. For the synthesis of 9'-substituted noscapine ionic liquids, the starting material 9'-bromo noscapine (**1**) was synthesized from α-noscapine by slightly modifying conditions published in the literature[56]. As depicted in Scheme 1, we then coupled various aryl boronic acids with the obtained 9'-bromo noscapine (**1**) in presence of $Pd(PPh_3)_4$ and aqueous Na_2CO_3under continuous refluxing of the solvents at 120 ℃ to produce 9'-substitituted suzuki-coupled noscapine analogues. Furthermore, these analogues were methylated at the respective nitrogen(s) using methyl iodide to form the organic cation of the anticipated APIL-ILs. Also, the rationale behind the choice of Iodide as the counter anion was the fact that it is an imperative micronutrient present naturally in the human body[57].

As documented in the literature, Structure activity relationship (SAR) analysis[58] of anticancer compounds indicate that electron-withdrawing functional group substitutions are predominantly more active than the electron-donating group substitutions. Additionally, para-substituted analogues are reported to be more bioactive compared to substitutions at other positions. Figure 2a shows the docking profile of all synthesized API-ILs with tubulin (target protein). Figure 2b displays the cytotoxicity (anticancer activity) profile of all API-ILs against H1299 (non-small lung cancer) cells. From Fig. 2b, we noted that 3 out of 4 derivatives with electron-withdrawing functional groups had better activity after 72 h, compared to the other ionic liquids. Interestingly, the bioactivity of compound 3b (electron-donating and para-substituted) differed with respect to its docking score profile. Also compound 3e had a low docking score & less activity despite being an electron-withdrawing substituted derivative. These differences may be attributed to previously reported observations that anticancer activity is an outcome of the combined effect of *para*-substitution and electron withdrawing group substitution rather than a sole factor. Overall, the profiles in Fig. 2a and b complement each other yielding [*p*-NO_2-Nos]I as the most potential anticancer agent amongst the obtained API-ILs with highest docking score of −10.0 $kcalmol^{-1}$ and highest bioactivity (least cell viability).

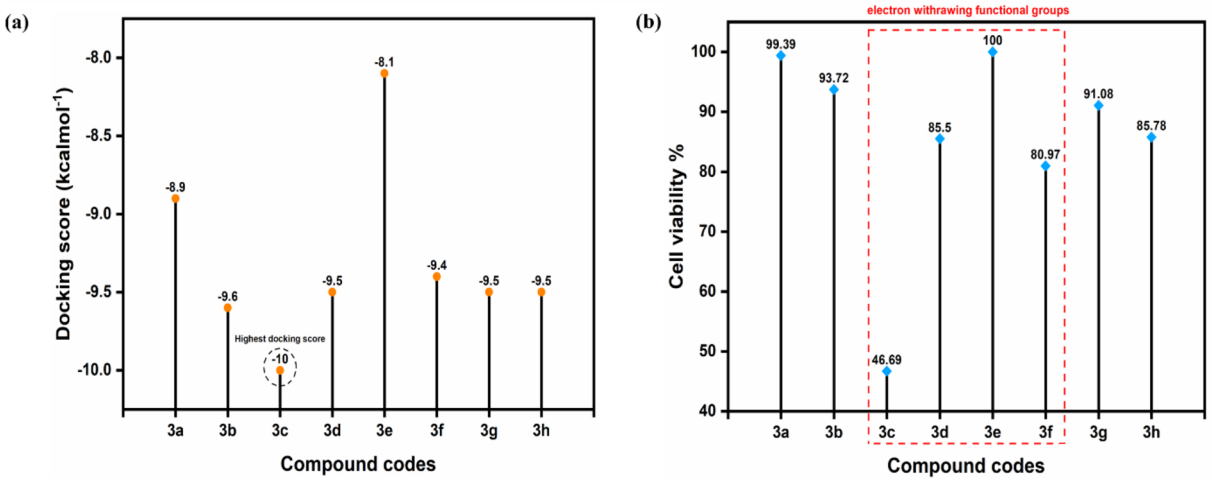

Fig. 2. (**a**) Docking scores with tubulin protein; (**b**) Cytotoxicity against H1299 cell line after 72 h (at 150 µM concentration), for all the synthesized API-ILs.

In the onward sections, we have discussed the molecular docking of all API-ILs with tubulin followed by molecular simulations and binding free energy calculations for [*p*-NO_2-Nos]I-tubulin complex. Thereon, we investigated binding interactions between human hemoglobin and [*p*-NO_2-Nos]I using spectroscopic methods. At last, we have compared the biological activity of noscapine, [9-Br-Nos]IBr_2 and [*p*-NO_2-Nos]I against non-small cell lung cancer.

In-silico evaluation: interaction with tubulin

Molecular docking and MD simulations

The visualization of possible interactions between protein and drug i.e., [*p*-NO_2-Nos]I is essential to better understand the most probable binding site(s) present in the 3D protein structure and probe into different types of interactions in the presence of drug at the atomic level. Molecular docking and molecular dynamics are promising and most frequently used methods to investigate such interactions. Autodock Vina V1.2.3 was used to calculate the binding energies of the synthesized ionic liquids with the 3D structure of tubulin (PDB – 1TUB) and the corresponding docking scores of their lowest energy conformation(s) are listed in Table 1 below.

From Table 1, we can infer that the highest binding energy or lowest energy conformation was found to be −10.0 $kcalmol^{-1}$ for [*p*-NO_2-Nos]I. The 3D polar interactions of the most potent [*p*-NO_2-Nos]I-tubulin complex are shown in Fig. 3a and Figs. 2d and 3b interactions are shown in the supporting information (Figure S34). The obtained complex was further used for MD simulation. MD simulation is crucial to analyze the stability of the formed complex under different reaction conditions. MD simulations were performed for a time span of 10 nanoseconds (ns)/ 10,000 picoseconds (ps) using the lowest energy complex obtained from molecular docking and the trajectories then obtained from MD were examined to report the occurring conformational changes throughout the simulation, frame by frame.

Using the final trajectories, RMSD (root mean square deviations) and RMSF (root mean square fluctuations) were calculated to examine the conformational flexibility in the protein structure at normal temperature and pressure conditions. As we can see in Fig. 4a, the RMSD values of the system (complex formed) did not change throughout the simulation after 4000 ps showing that the system attained equilibrium at 4000 ps. We thus inferred that [*p*-NO_2-Nos]I-tubulin complex is stable as it didn't deviate from the equilibrium. It was further confirmed from the stabilized fluctuations from Fig. 4b. During 3000 ps to 4000 ps, the RMSD values (Fig. 4a) were slightly stabilized which can be attributed to maximum number of H-bonds in this time frame during the simulation. The plot for hydrogen bond analysis of the simulation is shown in the supporting information (Figure S35).

Solvent Accessible Surface Area (SASA) analysis aided in understanding the compactness of the protein using area covered by either solvent or ligand/drug[59]. An increase in SASA signals rigidity in the system and a decrease means compactness in the structure of the protein. From Fig. 4c, we can see that the area increases a little from 0 ps to 2000 ps and then decreases later. This trend suggested that the system was initially covered by the solvent rather than the drug but subsequent decrease in area or increased compactness in the structure of protein implied interaction of [*p*-NO_2-Nos]I with tubulin.

In addition, Radius of gyration (Rg) can be defined as the mass-weighted root mean square deviations of the collection of atoms from their ground state of mass. A study of the Rg provides an understanding of the overall deviation in protein dimension namely deviation in secondary structure of the protein from its ground state. As we can see in Fig. 4d, Rg of the system increases till 2000 ps indicating change in protein structure (decreased compactness) and then later the system attained equilibrium stabilizing the fluctuations. This observation further assured the stability of [*p*-NO_2-Nos]I-tubulin complex formed throughout the MD simulation.

S.No.	Code	Structure of ionic liquid	Docking score (kcalmol^{-1})
1.	3a	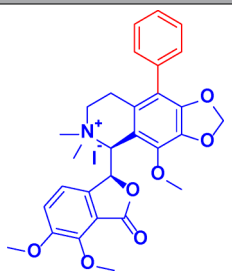	−8.9
2.	3b	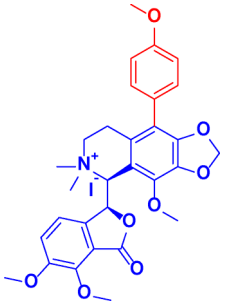	−9.6
3.	3c	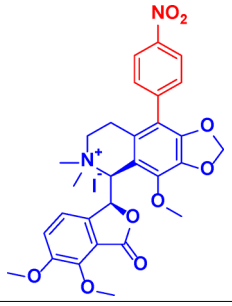	**−10.0**
4.	3d	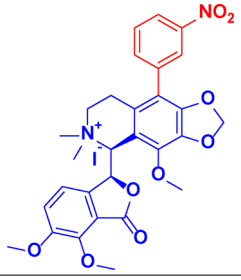	−9.5
5.	3e	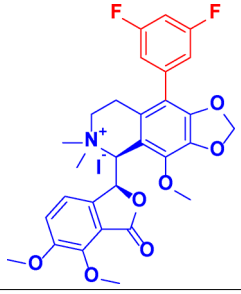	−8.1
Continued			

S.No.	Code	Structure of ionic liquid	Docking score (kcalmol^{-1})
6.	3f	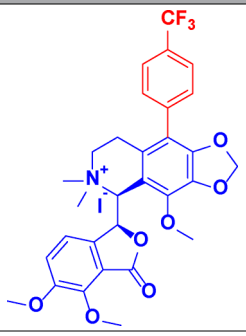	−9.4
7.	3g	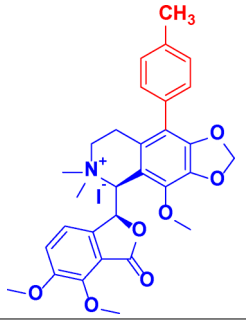	−9.5
8.	3h	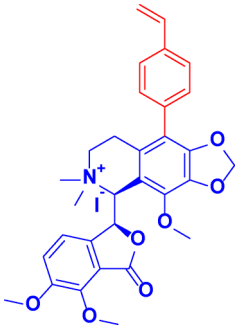	−9.5
9.	Noscapine	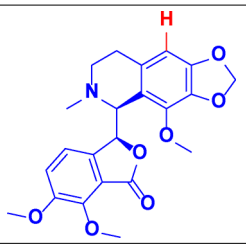	−8.7

Table 1. Molecular Docking scores of synthesized ionic liquids with tubulin.

Binding free energy MMPBSA/GBSA calculations

The MMPBSA/GBSA is another useful method to calculate the binding free energies of the ligands under assessment. The binding free energy analysis has been executed with the MM-PBSA/GBSA approach for the trajectories obtained from MD simulations during a period of 10 ns. The detailed Poisson Boltzmann analysis is listed in Table 2 and Generalized Born analysis in Table 3.

From MM-PBSA and MM-GBSA analysis, we can see that the net change is binding free energy for [*p*-NO_2-Nos]I-tubulin complex was negative (−19.18 kcalmol^{-1} and − 24.77 kcalmol^{-1} respectively). This signaled that the complex formation was a favorable or feasible process. From the obtained results, it is also visible that intermolecular Vander Waals (VDWAALS) and non-polar solvation (ENPOLAR) representing the burial of solvent accessible surface area favored the binding process whereas polar solvation (EPB) completely countered it. On the other hand, although the electrostatic interactions (EEL) and Gas phase electrostatic value (GGAS) contributed in favor of binding but overall electrostatic interaction energy (EEL + EPB/GB) was positive. This positive value can be due to the large desolvation penalty for charged and polar groups and on comparison, we concluded that the overall binding process was propelled by non-polar interactions.

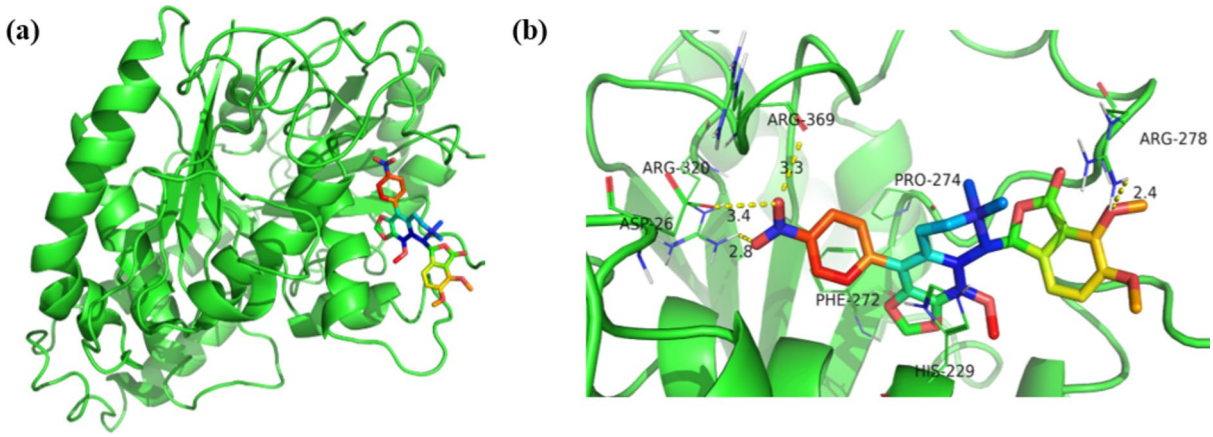

Fig. 3. Three dimensional docked poses of (**a**) [*p*-NO_2-Nos]I-tubulin interactions (**b**) Zoomed-in view of the docked complex.

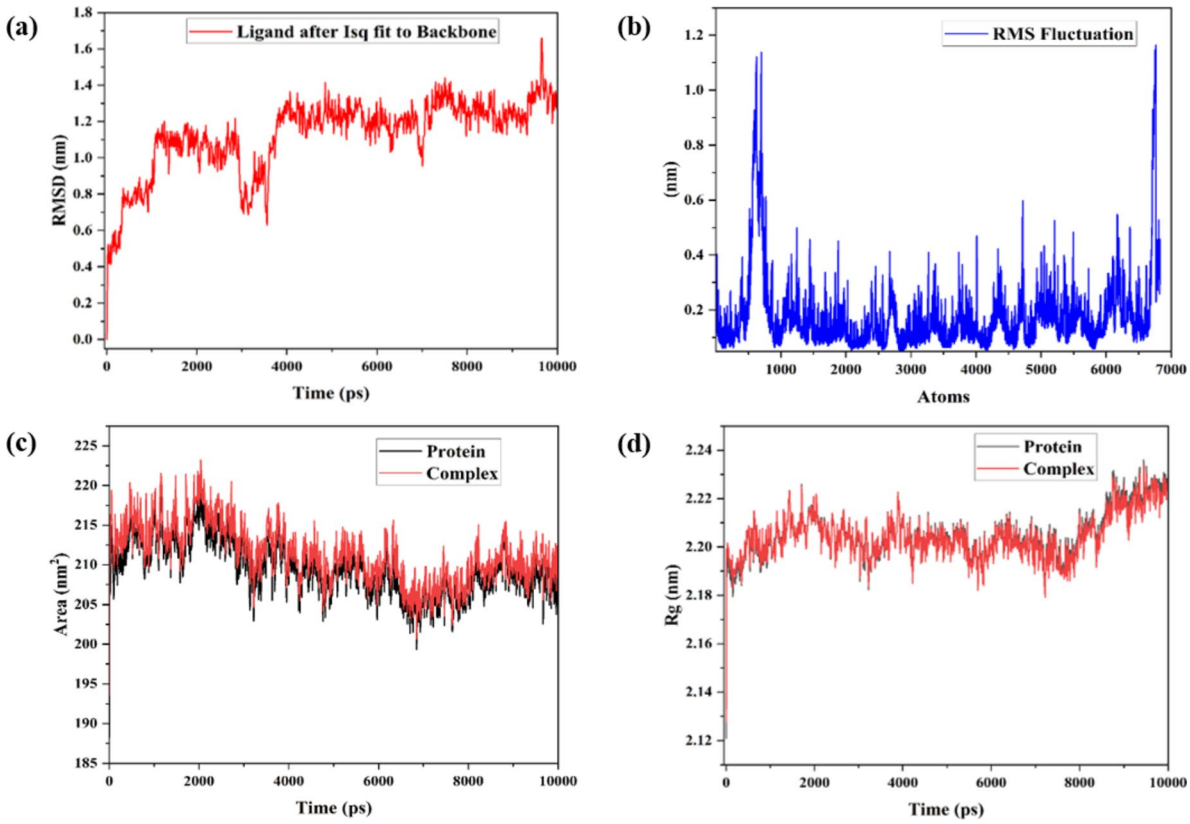

Fig. 4. MD simulation results of [*p*-NO_2-Nos]I-tubulin complex depicting (**a**) Root mean square deviation (RMSD); (**b**) Root mean square fluctuation (RMSF); (**c**) Solvent accessible area analysis (SASA); and (**d**) Radius of gyration.

Spectroscopic evaluation: biophysical interaction with Hb

Absorption spectral studies

Herein, UV-Visible Absorption spectroscopy is a conventional choice for understanding the drug-protein interactions because both α and β bands along with the soret band in hemoglobin are susceptible to even the slightest of structural modifications[60]. Hemoglobin displays a strong absorption spectrum due to its highly energetic electronic transitions in amino acid residues and the heme prosthetic group[61]. Amongst the three characteristic absorption peaks at 212, 272 and 406 nm (in the range of 200–500 nm), the peak at $\lambda_{max} = 212$ nm accounts for the α-helical backbone of the protein (n to π* transitions of the carbonyl groups (>C=O in the peptide chain); $\lambda_{max} = 272$ nm is attributed to the aryl amino acid residues (π to π* transitions in tryptophan,

Energy component	Complex*	Receptor*	Ligand*	ΔG_{bind}* (Complex – (Receptor + Ligand))
BOND	1334.75	1317.09	17.66	0
ANGLE	3527.44	3481.37	46.07	0
DIHED	4410.89	4373.76	37.13	0
VDWAALS	−3358.68	−3321.08	−9.07	−28.53
EEL	−28433.14	−28232.95	8.14	−208.33
1–4 VDW	1585.38	1572.40	12.98	0
1–4 EEL	18213.88	18158.69	55.19	0
EPB	−7350.24	−7506.09	−64.83	220.68
ENPOLAR	105.72	104.90	3.81	−2.99
EDISPER	0.00	0.00	0	0
GGAS	−2719.50	−2650.73	168.1	−236.87
GSOLV	−7244.52	−7401.19	−61.03	217.69
Total	−9964.02	−10051.92	107.07	−19.18

Table 2. Molecular mechanics Poisson Boltzmann surface area (MM-PBSA) analysis. *All units are reported in kcalmol^{-1} unless stated otherwise.

Energy Component	Complex*	Receptor*	Ligand*	ΔG_{bind}* (Complex – (Receptor + Ligand))
BOND	1334.75	1317.09	17.66	0
ANGLE	3527.44	3481.37	46.07	0
DIHED	4410.89	4373.76	37.13	0
VDWAALS	−3358.68	−3321.08	−9.07	−28.53
EEL	−28433.1	−28,233	8.14	−208.33
1–4 VDW	1585.38	1572.4	12.98	0
1–4 EEL	18213.88	18158.69	55.19	0
EGB	−7322.69	−7470.24	−68.19	215.73
ESURF	165.28	164.54	4.37	−3.63
GGAS	−2719.5	−2650.73	168.1	−236.87
GSOLV	−7157.42	−7305.7	−63.81	212.1
Total	−9876.91	−9956.43	104.29	−24.77

Table 3. Molecular mechanics generalized born surface area (MM-GBSA) analysis. *All units are reported in kcalmol^{-1} unless stated otherwise

tyrosine and phenylalanine) and λ_{max} = 406 nm denotes the Soret/heme band of porphyrin[27,62]. At 272 nm, we observed a hyperchromic shift upon gradually increasing the concentration of [*p*-NO_2-Nos]I compared to slight change at 406 nm (Fig. 5a). We inferred that there is potential interaction/complex formation between the ionic liquid and Hb owing to the orderly increase in absorption intensity. Also, the notable change at 272 nm relative to the negligible change at 406 nm suggests an alteration in the microenvironment of Hb around the aromatic amino acids rather than heme[63]. From Fig. 5b, we can see that [p-NO_2-Nos]I exhibits absorption maxima at 242 nm and 306 nm.

Fluorescence spectral studies

As a result of the intrinsic fluorescence of proteins, fluorescence spectroscopy has become a vital tool to assess the binding between proteins and drugs. It can be used to comprehend the binding mechanism and then later calculate the binding and thermodynamic parameters. Human Hemoglobin contains a total of six tryptophan residues (two α-Trp14, two β-Trp15 and two β-Trp37)[64] alongside other aromatic amino acid residues. Amongst them, β-Trp37 which is present at the $\alpha_1\beta_2$interface of Hb is the dominant contributor in its intrinsic fluorescence[65–67]. β-Trp37 is highly sensitive to interactions with small molecules/prospective quenchers due to its solvent exposure, and thus drug-protein binding leads to fluorescence quenching. In the absence of ionic liquid, Hb exhibits an emission maximum at 342 nm upon excitation at 280 nm whereas on addition of gradually increasing concentrations of [*p*-NO_2-Nos]I to Hb, we noted that the emission intensity decreases coupled with a bathochromic shift of λ = 4 nm (Fig. 6a). Similar trends can be seen in Fig. 6b and c too. These observations indicate that [*p*-NO_2-Nos]I and Hb are interacting in the vicinity of β-Trp37 residue plus an increased hydrophilic microenvironment around fluorescent amino acid residues in the protein.

Consequent upon spotting quenching in all emission spectra (298 K, 303 K and 308 K), we used this data to further scrutinize and ensure the quenching mechanism. (Fig. 7a)[68]. There are three types of fluorescence quenching for proteins namely static, dynamic, and mixed quenching. Static quenching occurs when there is complex formation between the fluorophore (protein) and quencher (drug); dynamic quenching is when there

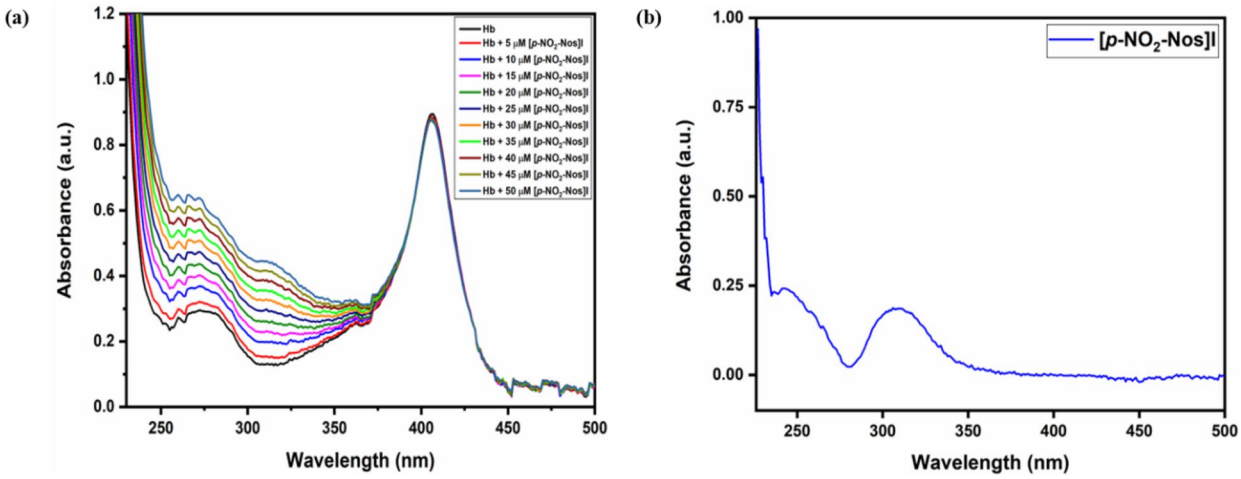

Fig. 5. UV-Visible absorption spectra of (**a**) Hb against different concentrations of [*p*-NO_2-Nos]I; (**b**) [*p*-NO_2-Nos]I (20 μM) exhibiting maxima at 242 nm and 306 nm.

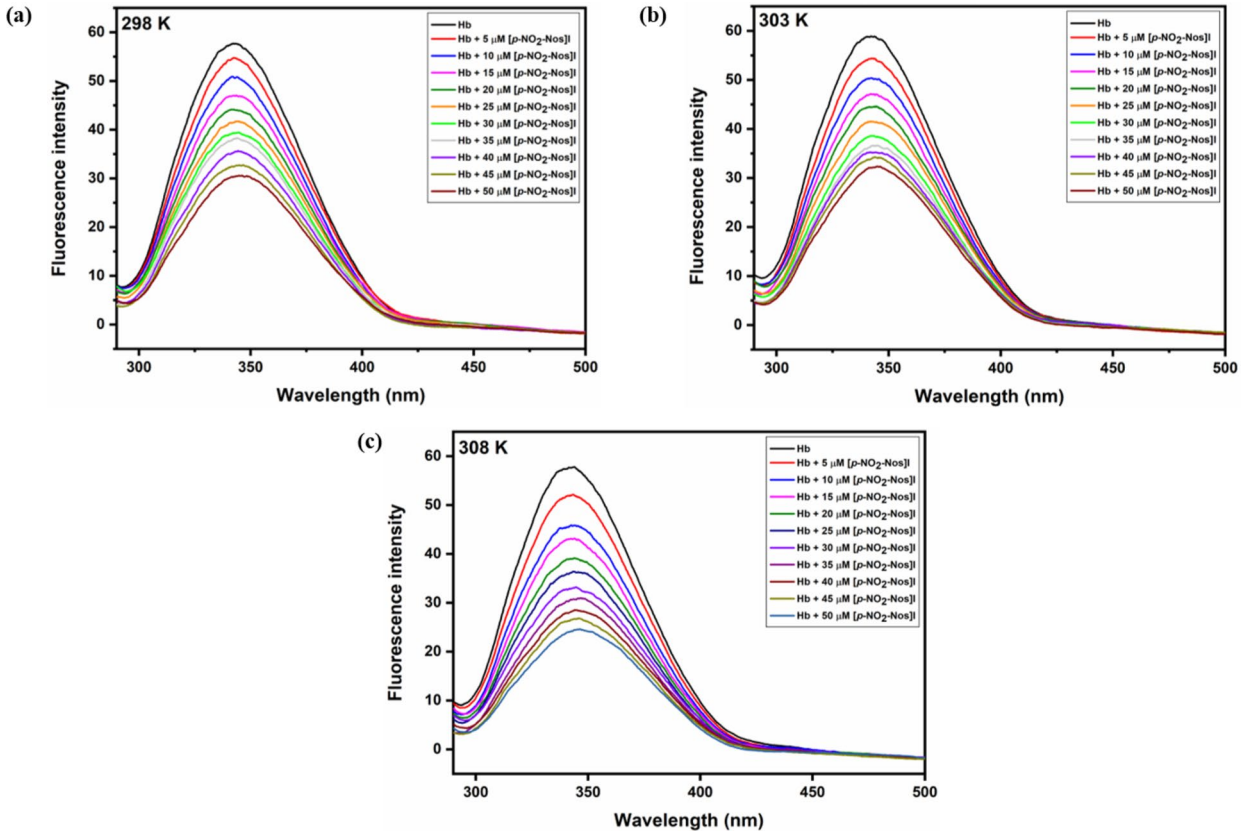

Fig. 6. Emission spectra of Hb against different concentrations of *[p*-NO_2-Nos]I at (**a**) 298 K; (**b**) 303 K; and (**c**) 308 K.

are collisional encounters amid fluorophore and quencher; and mixed quenching is an outcome of both the processes betiding together. From the three equations mentioned below, we can see that the dependance of F_0/F on *[Q]* is linear for dynamic (Eq. 5) and static quenching (Eq. 6) whereas it is non-linear for mixed quenching (Eq. 7)[68–70].

$$\frac{\mathrm{F_o}}{F} = 1 + \mathrm{K}_{sv}\,[Q] = \mathrm{K}_q \tau_o\,[Q] \tag{5}$$

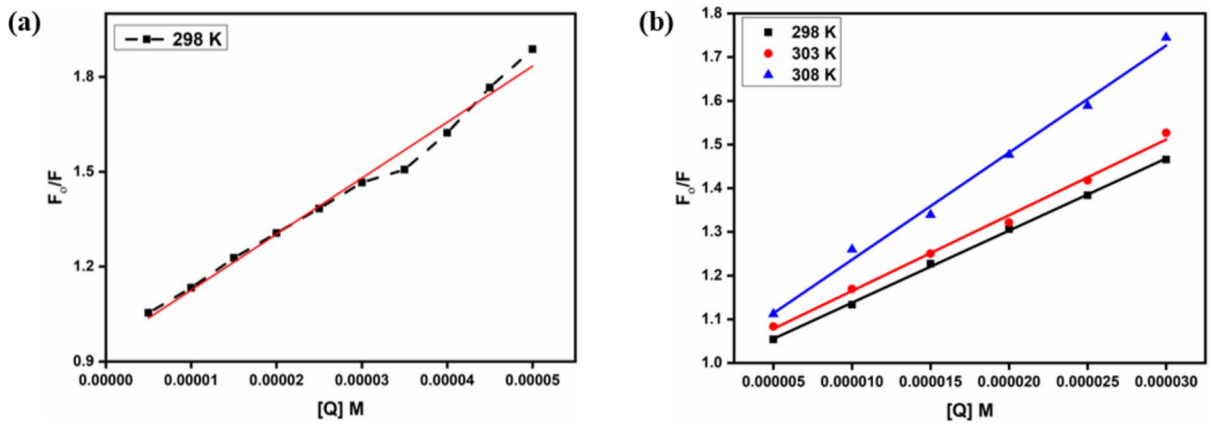

Fig. 7. Stern Volmer plot of Hb against different concentrations of (**a**) [*p*-NO_2-Nos]I at 298 K; (**b**) [*p*-NO_2-Nos]I (0 to 30 µM) at 298 K, 303 K and 308 K.

Temperature (K)	K_{sv} (M^{-1}) × 10^4	K_q ($M^{-1}s^{-1}$) × 10^{12}
298	1.6509	1.6509
303	1.7327	1.7327
308	2.4507	2.4507

Table 4. Stern Volmer and bimolecular quenching constants for [*p*-NO_2-Nos]I-Hb binding.

$$\frac{F_o}{F} = 1 + K_s [Q] \tag{6}$$

$$\frac{F_o}{F} = (1 + K_D [Q])(1 + K_S [Q]) \tag{7}$$

Herein, F and F_o are the fluorescence intensities of Hb in presence and absence of [*p*-NO_2-Nos]I, *[Q]* is the concentration of quencher, K_{sv} denotes the Stern-Volmer quenching constant, K_q denotes the bimolecular quenching constant, K_S is static quenching constant or association constant, K_D is dynamic quenching constant and τ_o (~ 10^{-8}seconds)[64,71] corresponds to the lifetime of Hb in absence of quencher.

From Fig. 7a, we can notice that the F_o/F against *[Q]* plot is non-linear (upward curvature, concave towards the y-axis) for drug concentrations from 0 to 50 µM indicating mixed quenching. To assure the quenching mechanism, we used the Stern-Volmer equation for the quencher concentration range of 0 to 30 µM (Fig. 7b) and then calculated K_{sv} and K_q (listed in Table 4). We spotted that the K_{sv} and K_q values for Hb increase with increasing temperatures insinuating dynamic quenching but concurrently K_q values are in the order of ~ 10^{12} $M^{-1}s^{-1}$ suggesting static quenching (2×10^{10} $M^{-1}s^{-1}$ is the maximum scattering collisional quenching constant for dynamic quenching). Thus, we deduced that [*p*-NO_2-Nos]I induced Hb quenching is mixed quenching[69,72–74] (prominently static along with dynamic quenching) in nature.

Subsequently, we employed the modified Stern-Volmer (Eq. 8) to calculate the binding constant and number of binding sites for the complex formed[69]. The modified Stern-Volmer plot for [*p*-NO_2-Nos]I-Hb binding is shown in Fig. 8a.

$$log\left(\frac{F_o - F}{F}\right) = \log K_b + n \log [Q] \tag{8}$$

Herein, K_b is the binding constant and n corresponds to the number of binding sites. The respective values obtained from the slopes (n) and intercepts ($\log K_b$) in Fig. 8a are listed in Table 5. From Table 5, we observed that $n \sim 1$ insinuating that [*p*-NO_2-Nos]I and Hb bind in a stoichiometric ratio of 1:1. Also, the binding constant was found to be 1.38×10^5 M^{-1} at 298 K. To further characterize the nature of interaction, we used the van't Hoff's plot (Fig. 8b) to obtain the related thermodynamic parameters using Eqs. 9 and 10.

$$\ln K_b = -\frac{\Delta H}{RT} + \frac{\Delta S}{R} \tag{9}$$

$$\Delta G = \Delta H - T\Delta S \tag{10}$$

In these equations, R denotes the universal gas constant (8.314 $Jmol^{-1}K^{-1}$), ΔG is the change in Gibb's free energy, ΔH is change in enthalpy and ΔS represents change in entropy.

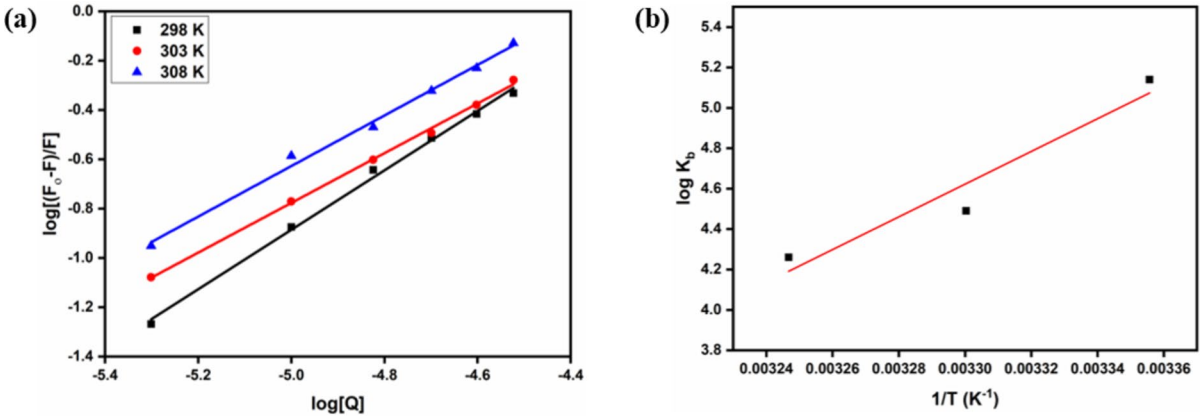

Fig. 8. (**a**) Modified Stern-Volmer's plot & (**b**) van't Hoffs plot; for [*p*-NO_2-Nos]I-Hb binding.

Temperature (Kelvin)	K_b (M^{-1})	*n*	Δ G (KJmol^{-1})	Δ H (KJmol^{-1})	Δ S (JK^{-1})
298	1.38×10^5	1.20	−28.949	−155.043	−423.132
303	30,903	1.00			
308	18,197	1.02			

Table 5. Thermodynamic parameters for [*p*-NO_2-Nos]I-Hb binding.

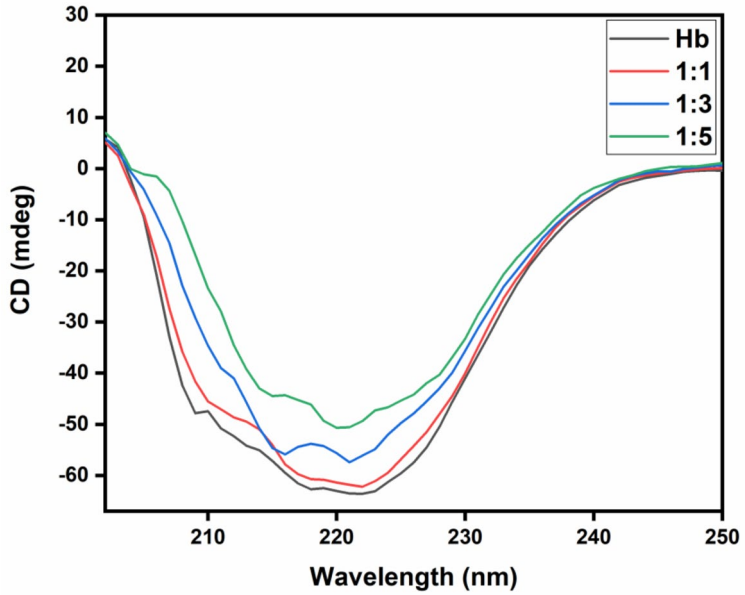

Fig. 9. Far-UV CD spectrum of Hb in presence and absence of [p-NO_2-Nos]I at 298 K.

From Table 5, we see that $\Delta G = -28.949$ KJmol^{-1} directing that the process is spontaneous. Also, the high negative values of values of ΔH *and* ΔS imply that hydrogen bonding and Van der Waals interactions are the main interacting forces during [*p*-NO_2-Nos]I-Hb complex formation[75].

Circular dichroism spectral studies

CD spectroscopy is a useful study to probe into [*p*-NO_2-Nos]I-Hb binding as it prioritizes structural alterations over physiochemical factors. Hemoglobin being a globular protein will lead to decrease in its α-helical content upon binding with the ionic liquid[76]. From Fig. 9, we can note that Hb displays two characteristic negative peaks at 208 nm and 228 nm in the far-UV CD spectrum at 298 K. The peak at 208 and 228 nm are accredited to π to π* and n to π* transitions respectively, thus marking the α-helical backbone of the tetrameric protein[77]. On progressively increasing [*p*-NO_2-Nos]I concentrations, there was an increase in the peak intensity as can

Secondary structures	Details of secondary structures	Percentage content of secondary structure			
		Hb	1:1	1:3	1:5
Helix		23.8	21.3	5.5	3.4
Antiparallel	Anti 1 (Left-twisted)	4.4	1.9	0.0	8.0
	Anti 2 (Relaxed)	0.0	0.0	7.5	8.9
	Anti 3 (Right twisted)	10.7	9.8	12.7	16.0
Parallel		9.4	11.5	14.7	11.6
Turns		16.0	15.2	12.6	10.7
Others		35.6	40.3	47.0	41.4

Table 6. Assessment of secondary structure of hb during [*p*-NO_2-Nos]I binding.

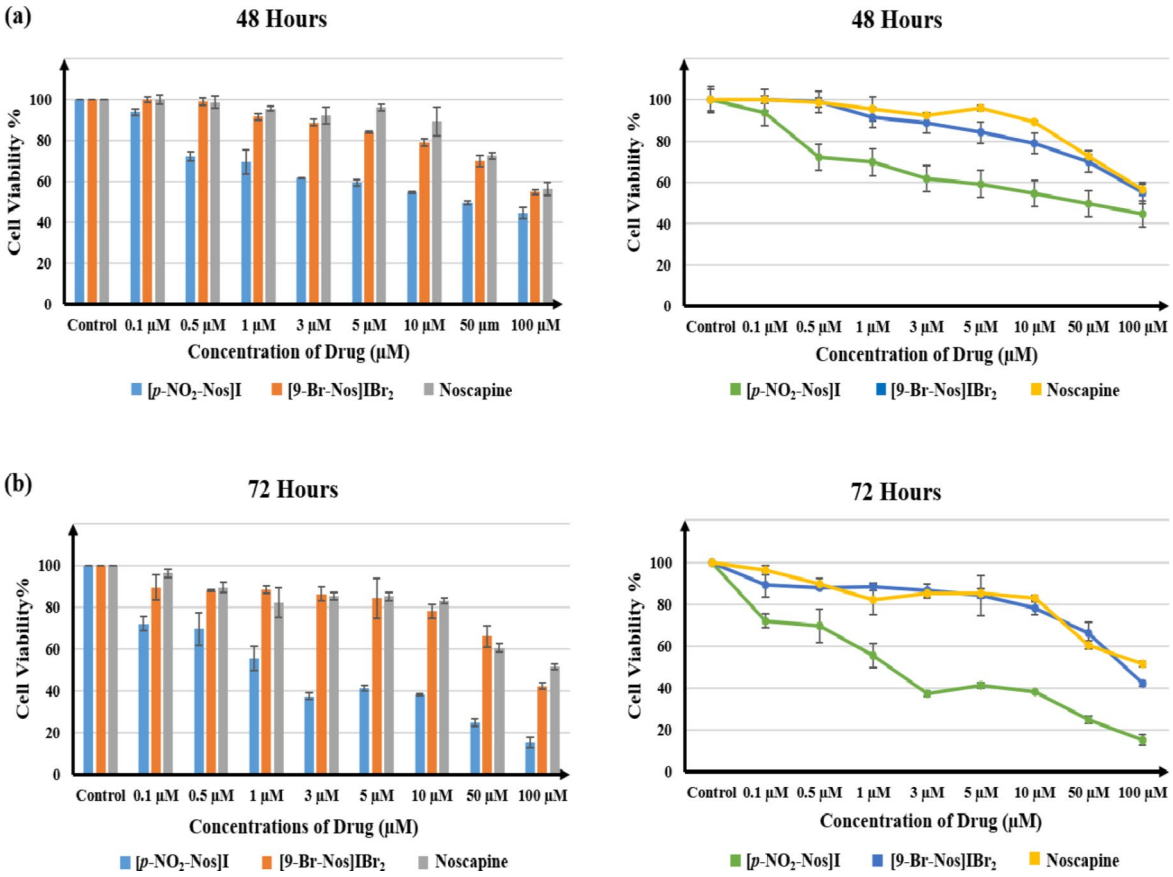

Fig. 10. Cytotoxicity profile of [*p*-NO_2-Nos]I, [9-Br-Nos]IBr_2 and Noscapine at (**a**) 48 h, and (**b**) 72 h.

be seen in Fig. 9. We then used BeStSel online server[78] to calculate the changes in secondary structure of Hb and the results for the same are listed in Table 6. We found that the α-helical content in pure Hb was 23.8% which decayed down to 3.4% in presence of the ionic liquid (Hb: [*p*-NO_2-Nos]I = 1:5) implying conformational changes in the secondary structure of Hb on binding with [*p*-NO_2-Nos]I.

Biological evaluation against cancer (H1299 and A549) cell line: MTT assay

To analyze the efficacy of the compelling API-IL i.e. [*p*-NO_2-Nos]I, we carried out in-vitro studies using the MTT assay. This colorimetric assay allowed us to comprehend the anti-proliferative activity of [*p*-NO_2-Nos]I, the parent compound - noscapine and 9-bromo noscapine ionic liquid - [9-Br-Nos]IBr_2 against H1299 (non-small cell lung cancer) cell line. The cytotoxicity profile (cell viability as a function of drug concentration) for all the compounds at 48 h and 72 h are shown in Fig. 10. The superiority of [*p*-NO_2-Nos]I over the parent compound and the previously reported [9-Br-Nos]IBr_2 is evident from their acquired IC_{50} values. At 48 h, the API-IL shows a lower $IC_{50} = 67.84 \pm 4.84$ µM compared to $IC_{50} = 105.52 \pm 11.45$ µM and 110.16 ± 6.34 µM of [9-Br-Nos]IBr_2 and noscapine respectively. At 72 h, [*p*-NO_2-Nos]I showed considerably better cytotoxic effect compared to its same corresponding concentration at 48 h which is clearly visible in Fig. 11. At 72 h, [*p*-NO_2-

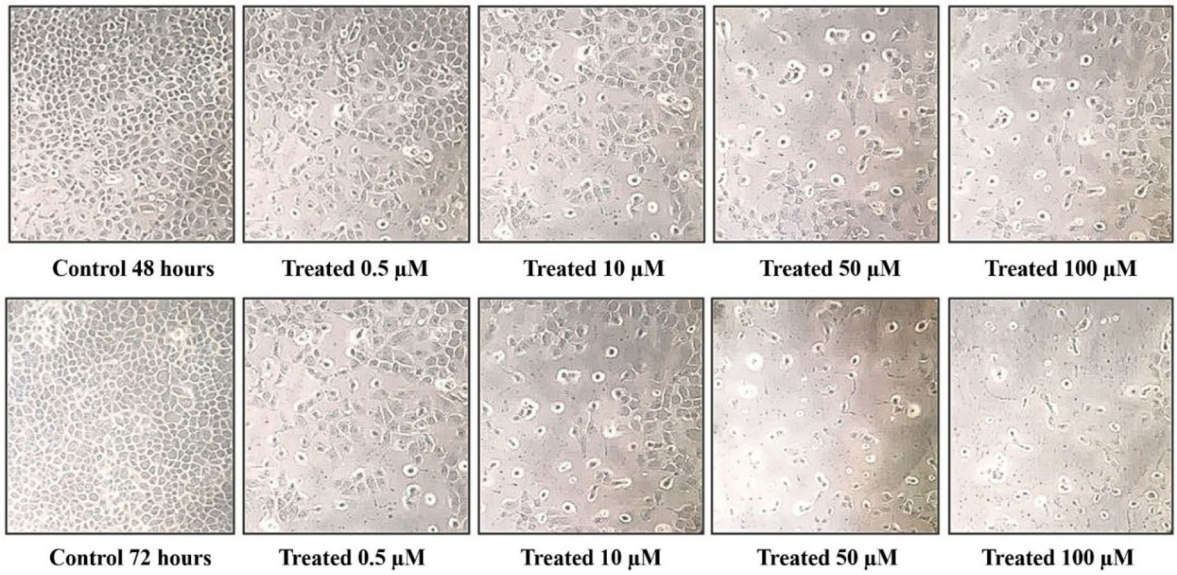

Fig. 11. Microscopic images of H1299 cells exposed to different concentrations of [*p*-NO_2-Nos]I at (**a**) 48 h, and (**b**) 72 h.

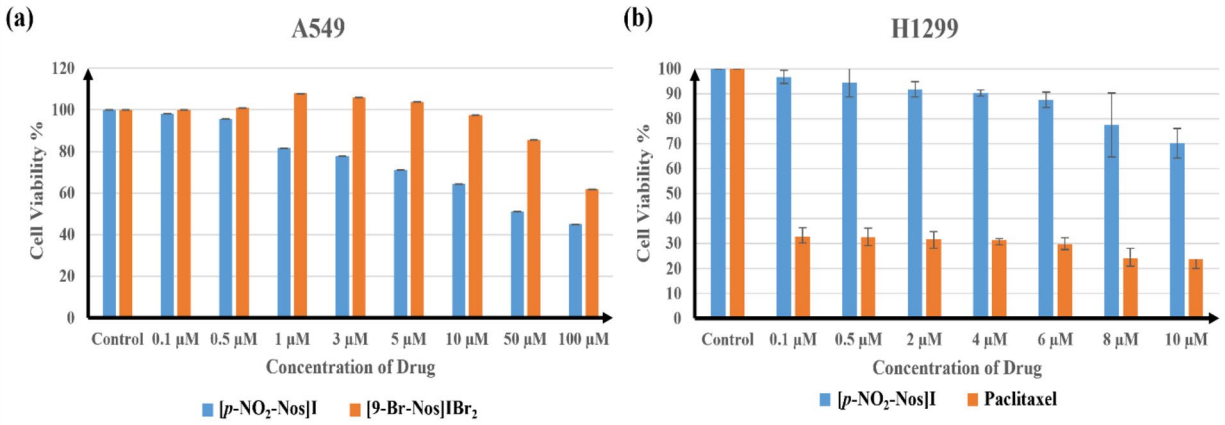

Fig. 12. Cytotoxicity profile of (**a**) [*p*-NO_2-Nos]I and Noscapine in A549 cell line; (**b**) [*p*-NO_2-Nos]I and Paclitaxel in H1299 cell line; after 48 h.

Nos]I shows a significantly lower $IC_{50} = 19.67 \pm 3.1$ µM relative to the $IC_{50} = 82.48 \pm 3.2$ µM of [9-Br-Nos]IBr_2 and $IC_{50} = 93.23 \pm 3.4$ µM of noscapine.

Next, we used the A549 cell line (another non-small cancer cell line) to further investigate the efficacy of the API-IL [*p*-NO_2-Nos]I relative to the parent compound. From Fig. 12a, we inferred that the result was similar in nature with respect to the cytotoxicity results in H1299 cell line. The IC_{50} values of both compounds were higher in A549 cell lines with [*p*-NO_2-Nos]I and noscapine having IC_{50} values of 73.88 ± 2.19 µM and 132.11 ± 6.65 µM, respectively. The lower IC_{50} values in H1299 cell line were in line with the general observed trend due to due to key biological and molecular differences between these two NSCLC (non-small cell lung cancer) cell lines. The lower IC_{50} values in H1299 cells are likely due to p53 deficiency, reduced drug efflux, faster proliferation, and weaker detoxification mechanisms, all of which make them more susceptible to drug-induced apoptosis.

Lastly, we compared the effectiveness of [*p*-NO_2-Nos]I against Paclitaxel which is a FDA-approved anticancer drug using H1299 cell line. From Fig. 12b, we noted that the IC_{50} of API-IL is 20-folds less relative to Paclitaxel after 48 h (IC_{50} of [*p*-NO_2-Nos]I and Paclitaxel was observed to be 19.24 ± 7.73 µM and 1.03 ± 3.07 µM, respectively). Given the relatively safer nature of noscapine and enhanced solubility of Noscapine-based ionic liquids compared to Paclitaxel, these derivatives hold the potential for further optimization in future studies.

Conclusion

Lung cancer is responsible for high death rates and huge socio-economic losses across international boundaries. Consequentially, the quest for anticancer agents continues with an emphasis on development of compounds that can disrupt critical cellular processes essential for tumor proliferation. Among widespread compounds under investigation, noscapine derivatives have acquired significant attention due to their inherent ability to bind to tubulin (a key protein involved in mitotic spindle formation). In this context, we have synthesized 9'-substituted suzuki -coupled noscapine ionic liquids representing a promising strategy to enhance the potency and efficacy of noscapine analogues against non-small cell lung cancer. We made use of the acclaimed suzuki-coupling to introduce the biaryl pharmacophore and later methylated the nitrogen to form the API-ILs which were thoroughly characterized. Using preliminary in silico and in vitro investigations, we then opted for the most potent API-IL which turned out to be [*p*-NO_2-Nos]I. This analogue was used for further assessments like interaction with the target tubulin protein using MD simulations and MM-PBSA/GBSA calculations, interaction with Hb using spectroscopic studies, and in-vitro screening using MTT assay. The computational studies showed that [*p*-NO_2-Nos]I-tubulin complex formation was a favorable process (stable complex formed) stimulated by non-polar interactions. The spectroscopic results revealed that [*p*-NO_2-Nos]I bind in a 1:1 stoichiometric ratio with Hb at 298 K with $K_b = 1.38 \times 10^5\ M^{-1}$. From in-vitro experiments, the relatively lower IC_{50} values obtained for [*p*-NO_2-Nos]I (67.84 ± 4.84 µM at 48 h and 19.67 ± 3.1µM at 72 h) signaled enhanced potency of these API-ILs against non-small cell lung cancer which were further supported by similar observed results in A549 cell line. These findings provide valuable insights into the therapeutic potential of such upgraded spindle poisons and its prospects for further development as a clinically viable anticancer agent.

Data availability

The data has been provided as supplementary information.

Received: 22 January 2025; Accepted: 13 March 2025
Published online: 30 September 2025

References

1. Bray, F. et al. Global cancer statistics 2022: GLOBOCAN estimates of incidence and mortality worldwide for 36 cancers in 185 countries. *CA Cancer J. Clin.* **74**, 229–263. https://doi.org/10.3322/caac.21834 (2024).
2. Olaussen, K. A. & Postel-Vinay, S. Predictors of chemotherapy efficacy in non-small-cell lung cancer: A challenging landscape. *Ann. Oncol.* **27**, 2004–2016. https://doi.org/10.1093/annonc/mdw321 (2016).
3. Fu, X. Y. et al. Three rounds of stability-guided optimization and systematical evaluation of oncolytic peptide LTX-315. *J. Med. Chem.* **67**, 3885–3908. https://doi.org/10.1021/acs.jmedchem.3c02232 (2024).
4. Yin, H. et al. The hybrid oncolytic peptide NTP-385 potently inhibits adherent cancer cells by targeting the nucleus. *Acta Pharmacol. Sin.* **44**, 201–210. https://doi.org/10.1038/s41401-022-00939-x (2023).
5. Yin, H. et al. Design, synthesis and anticancer evaluation of novel oncolytic peptide-chlorambucil conjugates. *Bioorg. Chem.* **138**, 106674. https://doi.org/10.1016/j.bioorg.2023.106674 (2023).
6. Dumontet, C. & Jordan, M. A. Microtubule-binding agents: A dynamic field of cancer therapeutics. *Nat. Rev. Drug Discov.* **9**, 790–803. https://doi.org/10.1038/nrd3253 (2010).
7. Newman, D. J. & Cragg, G. M. Natural products as sources of new drugs over the nearly four decades from 01/1981 to 09/2019. *J. Nat. Prod.* **83**, 770–803. https://doi.org/10.1021/acs.jnatprod.9b01285 (2020).
8. Rida, P. C. G., Livecche, D., Ogden, A., Zhou, J. & Aneja, R. The Noscapine chronicle: A Pharmaco-Historic biography of the opiate alkaloid family and its clinical applications. *Med. Res. Rev.* **35**, 1072–1096. https://doi.org/10.1002/med.21357 (2015).
9. Ye, K. et al. Opium alkaloid noscapine is an antitumor agent that arrests metaphase and induces apoptosis in dividing cells, (1998). www.pnas.org
10. Zhou, J., Panda, D., Landen, J. W., Wilson, L. & Joshi, H. C. Minor alteration of microtubule dynamics causes loss of tension across kinetochore pairs and activates the spindle checkpoint. *J. Biol. Chem.* **277**, 17200–17208. https://doi.org/10.1074/jbc.M110369200 (2002).
11. Ke, Y. et al. Noscapine inhibits tumor growth with little toxicity to normal tissues or Inhibition of immune responses. *Cancer Immunol. Immunother.* **49**, 217–225 (2000).
12. Jain, N. et al. Synthesis and antitumor evaluation of Nitrovinyl biphenyls: anticancer agents based on allocolchicines. *ChemMedChem* **6**, 859–868. https://doi.org/10.1002/cmdc.201100019 (2011).
13. Marzaro, G. et al. Discovery of biarylaminoquinazolines as novel tubulin polymerization inhibitors. *J. Med. Chem.* **57**, 4598–4605. https://doi.org/10.1021/jm500034j (2014).
14. Yu, F. L. et al. Discovery of novel antitumor dibenzocyclooctatetraene derivatives and related biphenyls as potent inhibitors of NF-κB signaling pathway. *Bioorg. Med. Chem.* **22**, 325–333. https://doi.org/10.1016/j.bmc.2013.11.018 (2014).
15. Porcù, E. et al. Novel 9′-substituted-noscapines: synthesis with Suzuki cross-coupling, structure Elucidation and biological evaluation. *Eur. J. Med. Chem.* **84**, 476–490. https://doi.org/10.1016/j.ejmech.2014.07.050 (2014).
16. Dash, S. G., Suri, C., Nagireddy, P. K. R., Kantevari, S. & Naik, P. K. Rational design of 9-vinyl-phenyl Noscapine as potent tubulin binding anticancer agent and evaluation of the effects of its combination on docetaxel. *J. Biomol. Struct. Dyn.* **39**, 5276–5289. https://doi.org/10.1080/07391102.2020.1785945 (2021).
17. Santoshi, S. et al. Rational design of biaryl pharmacophore inserted Noscapine derivatives as potent tubulin binding anticancer agents. *J. Comput. Aided Mol. Des.* **29**, 249–270. https://doi.org/10.1007/s10822-014-9820-5 (2015).
18. Zhuang, W. et al. Ionic liquids in pharmaceutical industry: A systematic review on applications and future perspectives. *J. Mol. Liq.* **349** https://doi.org/10.1016/j.molliq.2021.118145 (2022).
19. Pedro, S. N., Freire, C. S. R., Silvestre, A. J. D. & Freire, M. G. Ionic liquids in drug delivery. *Encyclopedia* **1**, 324–339. https://doi.org/10.3390/encyclopedia1020027 (2021).
20. Hough, W. L. et al. The third evolution of ionic liquids: active pharmaceutical ingredients. *New J. Chem.* **31**, 1429–1436. https://doi.org/10.1039/b706677p (2007).
21. Egorova, K. S., Gordeev, E. G. & Ananikov, V. P. Biological activity of ionic liquids and their application in pharmaceutics and medicine. *Chem. Rev.* **117**, 7132–7189. https://doi.org/10.1021/acs.chemrev.6b00562 (2017).
22. Dias, A. R., Costa-Rodrigues, J., Fernandes, M. H., Ferraz, R. & Prudêncio, C. The Anticancer Potential of Ionic Liquids, ChemMedChem 12 11–18. (2017). https://doi.org/10.1002/cmdc.201600480

23. Sewariya, S. et al. Comparative assessment of 9-bromo Noscapine ionic liquid and Noscapine: synthesis, in-vitro studies plus computational & biophysical evaluation with human hemoglobin. *Int. J. Biol. Macromol.* **247** https://doi.org/10.1016/j.ijbiomac.2023.125791 (2023).
24. Vijayan, V., Uthaman, S. & Park, I. K. Cell membrane-camouflaged nanoparticles: A promising biomimetic strategy for cancer theragnostics. *Polym. (Basel)*. 10. https://doi.org/10.3390/polym10090983 (2018).
25. Tian, H. et al. Cancer cell Membrane-Biomimetic oxygen nanocarrier for breaking Hypoxia-Induced chemoresistance. *Adv. Funct. Mater.* **27** https://doi.org/10.1002/adfm.201703197 (2017).
26. Biagiotti, S., Pirla, E. & Magnani, M. Drug transport by red blood cells. *Front. Physiol.* **14** https://doi.org/10.3389/fphys.2023.1308632 (2023).
27. Sehrawat, H. et al. Unraveling the interaction of an opium poppy alkaloid Noscapine ionic liquid with human hemoglobin: biophysical and computational studies. *J. Mol. Liq.* **338** https://doi.org/10.1016/j.molliq.2021.116710 (2021).
28. Sehrawat, H. et al. Mechanistic interaction of triflate based Noscapine ionic liquid with BSA: spectroscopic and chemoinformatics approaches. *J. Mol. Liq.* **315** https://doi.org/10.1016/j.molliq.2020.113695 (2020).
29. Sehrawat, H., Kumar, N., Panchal, S., Kumar, L. & Chandra, R. Imperative persistent interaction analysis of anticancer noscapine-ionic liquid with calf thymus DNA. *Int. J. Biol. Macromol.* **220**, 415–425. https://doi.org/10.1016/j.ijbiomac.2022.08.106 (2022).
30. Panchal, S., Sehrawat, H., Sharma, N. & Chandra, R. Biochemical interaction of human hemoglobin with ionic liquids of noscapinoids: spectroscopic and computational approach. *Int. J. Biol. Macromol.* **239** https://doi.org/10.1016/j.ijbiomac.2023.124227 (2023).
31. Trott, O. & Olson, A. J. AutoDock Vina: improving the speed and accuracy of Docking with a new scoring function, efficient optimization, and multithreading. *J. Comput. Chem.* **31**, 455–461. https://doi.org/10.1002/jcc.21334 (2010).
32. AllingerN. L. Conformational analysis. 130. MM2. A hydrocarbon force field utilizing V1 and V2 torsional terms. *J. Am. Chem. Soc.* **99** (25), 8127–8134 (1977).
33. Nogales, E., Wolf, S. G. & Downing, K. H. Structure of the tubulin dimer by electron crystallography, (1998).
34. Berman, H. M. et al. Protein Data Bank. *Nucleic Acids Res.* **28**, 235–242 (2000).
35. Biovia, D. S. et al. Dassault systèmes BIOVIA, discovery studio V.sualizer, V. 17.2, San Diego: Dassault systèmes, 2016. *J. Chem. Phys.* **10**, 21–9991 (2000).
36. DeLano, W. L. The PyMOL Molecular Graphics System, DeLano Scientific (2002).
37. Morris, G. M. et al. Software news and updates AutoDock4 and AutoDockTools4: automated Docking with selective receptor flexibility. *J. Comput. Chem.* **30**, 2785–2791. https://doi.org/10.1002/jcc.21256 (2009).
38. Bekker, H. J. C. et al. Gromacs-a parallel computer for molecular-dynamics simulations, In *4th international conference on computational physics (PC 92)*, World Scientific Publishing pp. 252–256. (1993).
39. Abraham, M. J. et al. Gromacs: high performance molecular simulations through multi-level parallelism from laptops to supercomputers. *SoftwareX* **1-2**, 19–25. https://doi.org/10.1016/j.softx.2015.06.001 (2015).
40. Páll, S., Abraham, M. J., Kutzner, C., Hess, B. & Lindahl, E. Tackling Exascale Software Challenges in Molecular Dynamics Simulations with GROMACS, (2015). http://link.springer.com/chapter/10
41. Pronk, S. et al. GROMACS 4.5: A high-throughput and highly parallel open source molecular simulation toolkit. *Bioinformatics* **29**, 845–854. https://doi.org/10.1093/bioinformatics/btt055 (2013).
42. Hess, B., Kutzner, C., Van Der Spoel, D. & Lindahl, E. GRGMACS 4: algorithms for highly efficient, load-balanced, and scalable molecular simulation. *J. Chem. Theory Comput.* **4**, 435–447. https://doi.org/10.1021/ct700301q (2008).
43. Van Der Spoel, D. et al. GROMACS: fast, flexible, and free. *J. Comput. Chem.* **26**, 1701–1718. https://doi.org/10.1002/jcc.20291 (2005).
44. Lindahl, E., Hess, B. & van der Spoel, D. GROMACS 3.0: A package for molecular simulation and trajectory analysis. *J. Mol. Model.* **7**, 306–317. https://doi.org/10.1007/S008940100045 (2001).
45. Berendsen, H. J. C., Van Der Spoel, D. & Van Drunen, R. GROMACS: A message-passing parallel molecular dynamics implementation PROGRAM SUMMARY Title of program: GROMACS version 1.0, (1995).
46. Lindorff-Larsen, K. et al. Improved side-chain torsion potentials for the amber ff99SB protein force field. *Proteins: Struct. Function Bioinf.* **78**, 1950–1958. https://doi.org/10.1002/prot.22711 (2010).
47. Wang, J., Wang, W., Kollman, P. A. & Case, D. A. Antechamber, An Accessory Software Package For Molecular Mechanical Calculations Correspondence to, n.d.
48. Silva, D. & Vranken, B. F. ACPYPE-AnteChamber PYthon Parser interfacE, (2012). http://www.biomedcentral.com/1756-0500/5/367
49. Wang, J., Wolf, R. M., Caldwell, J. W., Kollman, P. A. & Case, D. A. Development and testing of a general amber force field. *J. Comput. Chem.* **25**, 1157–1174. https://doi.org/10.1002/jcc.20035 (2004).
50. Wang, J., Wang, W., Kollman, P. A. & Case, D. A. Automatic atom type and bond type perception in molecular mechanical calculations. *J. Mol. Graph Model.* **25**, 247–260. https://doi.org/10.1016/j.jmgm.2005.12.005 (2006).
51. Valdés-Tresanco, M. S., Valdés-Tresanco, M. E., Valiente, P. A. & Moreno, E. Gmx_MMPBSA: A new tool to perform End-State free energy calculations with GROMACS. *J. Chem. Theory Comput.* **17**, 6281–6291. https://doi.org/10.1021/acs.jctc.1c00645 (2021).
52. Wang, E. et al. End-Point binding free energy calculation with MM/PBSA and MM/GBSA: strategies and applications in drug design. *Chem. Rev.* **119**, 9478–9508. https://doi.org/10.1021/acs.chemrev.9b00055 (2019).
53. Genheden, S. & Ryde, U. The MM/PBSA and MM/GBSA methods to estimate ligand-binding affinities. *Expert Opin. Drug Discov.* **10**, 449–461. https://doi.org/10.1517/17460441.2015.1032936 (2015).
54. Wang, C., Greene, D., Xiao, L., Qi, R. & Luo, R. Recent developments and applications of the MMPBSA method. *Front. Mol. Biosci.* **4** https://doi.org/10.3389/fmolb.2017.00087 (2018).
55. Bai, L. & Wang, J. X. Environmentally Friendly Suzuki Aryl-Aryl Cross-Coupling Reaction, (2005).
56. Zhou, J. et al. Brominated derivatives of Noscapine are potent Microtubule-interfering agents that perturb mitosis and inhibit cell proliferation. *Mol. Pharmacol.* **3**, 799–807 (2003). http://molpharm.aspetjournals.org
57. Ahad, F. & Ganie, S. A. Iodine, iodine metabolism and iodine deficiency disorders revisited. *Indian J. Endocrinol. Metabol.* **14** (1), 13–17 (2010).
58. Liew, S. K., Malagobadan, S., Arshad, N. M. & Nagoor, N. H. A review of the structure—activity relationship of natural and synthetic antimetastatic compounds. *Biomolecules* **10** https://doi.org/10.3390/biom10010138 (2020).
59. by A. Bondi, THE JOURNAL OF PHYSICAL CHEMISTRY Registered in U. S. Patent Office© der Waals Volumes and Radii, UTC, 2024. https://pubs.acs.org/sharingguidelines.
60. Dimer, H. H., Nichols, W. L., Zimm, B. H., Ten, L. F. & Eyck Conformation-invariant Structures of the α1 β1 Human Hemoglobin Dimer, (1997).
61. Zagrean-Tuza, C., Igescu, I., Lupan, A. & Silaghi-Dumitrescu, R. A study of the molecular interactions of hemoglobin with diverse classes of therapeutic agents. *Inorganica Chim. Acta*. **567** https://doi.org/10.1016/j.ica.2024.122053 (2024).
62. Liu, W., Ding, F. & Sun, Y. Characterization of phenosafranine-hemoglobin interactions in aqueous solution. *J. Solut. Chem.* **40**, 231–246. https://doi.org/10.1007/s10953-010-9647-1 (2011).
63. Chugh, H. et al. Ex vivo binding studies of the anti-cancer drug Noscapine with human hemoglobin: a spectroscopic and molecular Docking study. *New J. Chem.* **45**, 1525–1534. https://doi.org/10.1039/d0nj03334k (2021).
64. Wang, Y. Q., Zhang, H. M. & Tang, B. P. The interaction of C.I. Acid red 27 with human hemoglobin in solution. *J. Photochem. Photobiol B.* **100**, 76–83. https://doi.org/10.1016/j.jphotobiol.2010.05.004 (2010).

65. Kritika, N. et al. Comparative analysis of Cobalt ferrite and iron oxide nanoparticles using bimodal hyperthermia, along with physical and in Silico interaction with human hemoglobin. *J. Mater. Chem. B.* **11**, 4785–4798. https://doi.org/10.1039/d2tb02447k (2023).
66. Hazra, S. & Suresh Kumar, G. Structural and thermodynamic studies on the interaction of Iminium and alkanolamine forms of sanguinarine with hemoglobin. *J. Phys. Chem. B.* **118**, 3771–3784. https://doi.org/10.1021/jp409764z (2014).
67. Alpert, B., Jameson, D. M. & E R E R, G. W. TRYPTOPHAN EMISSION FROM HUMAN HEMOGLOBIN AND ITS ISOLATED SUBUNITS, n.d.
68. Wang, Q. et al. Binding interaction of Atorvastatin with bovine serum albumin: spectroscopic methods and molecular Docking. *Spectrochim Acta Mol. Biomol. Spectrosc.* **156**, 155–163. https://doi.org/10.1016/j.saa.2015.12.003 (2016).
69. Zhang, Y. F., Zhou, K. L., Lou, Y. Y., Pan, D. Q. & Shi, J. H. Investigation of the binding interaction between Estazolam and bovine serum albumin: Multi-spectroscopic methods and molecular Docking technique. *J. Biomol. Struct. Dyn.* **35**, 3605–3614. https://doi.org/10.1080/07391102.2016.1264889 (2017).
70. K.A. Bostian, Instrumentation for Differential Fluorescence Spectroscopy, (1977).
71. Lakowicz, J. R. & Weber, G. *Quenching of Fluorescence by Oxygen. A Probe for Structural Fluctuations in Macromoleculest* (UTC, 1966). https://pubs.acs.org/sharingguidelines
72. Manna, A. & Chakravorti, S. Role of block copolymer-micelle nanocomposites in dye-bovine serum albumin binding: A combined experimental and molecular Docking study. *Mol. Biosyst.* **9**, 246–257. https://doi.org/10.1039/c2mb25368b (2013).
73. Tong, J. Q. et al. Probing the adverse temperature dependence in the static fluorescence quenching of BSA induced by a novel anticancer hydrazone. *Photochemical Photobiological Sci.* **11**, 1868–1879. https://doi.org/10.1039/c2pp25162k (2012).
74. Tian, F. F. et al. The adsorption of an anticancer hydrazone by protein: an unusual static quenching mechanism. *RSC Adv.* **2**, 501–513. https://doi.org/10.1039/c1ra00521a (2012).
75. Ross P. D. & Subramanian S. Thermodynamics of protein association reactions: forces contributing to Stability. *Biochemistry* **20**(11), 3096–3102. https://pubs.acs.org/sharingguidelines (1981).
76. Greenfield, N. J. Using circular dichroism spectra to estimate protein secondary structure. *Nat. Protoc.* **1**, 2876–2890. https://doi.org/10.1038/nprot.2006.202 (2007).
77. Corchnoy, S. B. et al. Intramolecular proton transfers and structural changes during the photocycle of the LOV2 domain of phototropin 1. *J. Biol. Chem.* **278**, 724–731. https://doi.org/10.1074/jbc.M209119200 (2003).
78. Micsonai, A. et al. BeStSel: A web server for accurate protein secondary structure prediction and fold recognition from the circular dichroism spectra. *Nucleic Acids Res.* **46**, W315–W322. https://doi.org/10.1093/nar/gky497 (2018).

Acknowledgements

R.C. is grateful to University of Delhi for providing lab facility. S.S. (Grant no. – 09/045 (1739)/2019-EMR-I) would like to thank Council of Scientific and Industrial Research (CSIR) for providing Senior Research Fellowship. All the authors are thankful to USIC, University of Delhi for providing instrumentation facilities.

Author contributions

Shubham Sewariya – Conceptualization, Methodology, Investigation, Data Curation, Writing-Original Draft, Visualization.Nistha Mishra – Methodology, Investigation, Data CurationSagar Panchal – Methodology, Investigation, Data CurationShrikant Kukreti – Validation, Resources, Supervision.Ramesh Chandra – Conceptualization, Validation, Resources, Writing-Review & Editing, Supervision, Funding Acquisition.

Declarations

Conflict of interest

The authors have no conflict of interest to declare.

Additional information

Supplementary Information The online version contains supplementary material available at https://doi.org/10.1038/s41598-025-94336-z.

Correspondence and requests for materials should be addressed to R.C.